

Effect of natural carbonation on the pore structure and elastic modulus of the alkali-activated fly ash and slag pastes

Nedeljkovic, M.; Savija, B.; Zuo, Yibing; Luković, Mladena; Ye, Guang

DOI

[10.1016/j.conbuildmat.2017.12.005](https://doi.org/10.1016/j.conbuildmat.2017.12.005)

Publication date

2018

Document Version

Accepted author manuscript

Published in

Construction and Building Materials

Citation (APA)

Nedeljkovic, M., Savija, B., Zuo, Y., Luković, M., & Ye, G. (2018). Effect of natural carbonation on the pore structure and elastic modulus of the alkali-activated fly ash and slag pastes. *Construction and Building Materials*, 161, 687-704. <https://doi.org/10.1016/j.conbuildmat.2017.12.005>

Important note

To cite this publication, please use the final published version (if applicable). Please check the document version above.

Copyright

Other than for strictly personal use, it is not permitted to download, forward or distribute the text or part of it, without the consent of the author(s) and/or copyright holder(s), unless the work is under an open content license such as Creative Commons.

Takedown policy

Please contact us and provide details if you believe this document breaches copyrights. We will remove access to the work immediately and investigate your claim.

1 **Effect of natural carbonation on the pore structure and elastic**
2 **modulus of the alkali-activated fly ash and slag pastes**

3 Marija Nedeljković^{a*}, Branko Šavija^{a,b}, Yibing Zuo^a, Mladena Luković^c,
4 Guang Ye^{a,d}

5 ^a Microlab, Faculty of Civil Engineering and Geosciences, Delft University of
6 Technology, Stevinweg 1, 2628 CN Delft, The Netherlands

7 ^b TNO Technical Sciences, Structural Reliability, Delft, The Netherlands

8 ^c Concrete Structures, Faculty of Civil Engineering and Geosciences, Delft University
9 of Technology, Stevinweg 1, 2628 CN Delft, The Netherlands

10 ^d Magnel Laboratory for Concrete Research, Department of Structural Engineering,
11 Ghent University Technologiepark-Zwijnaarde 904 B-9052, Ghent (Zwijnaarde), Belgium

12
13 e-mail: M.Nedeljkovic@tudelft.nl

14 B.Savija@tudelft.nl

15 Y.Zuo@tudelft.nl

16 M.Lukovic@tudelft.nl

17 G.Ye@tudelft.nl

18
19 * Corresponding author

20 Tel: +31(0)15 27 82290

21
22
23 **ABSTRACT**

24 The aim of this paper was to investigate the effect of natural carbonation on the pore
25 structure, and elastic modulus (E_m) of alkali-activated fly ash (FA) and ground granulated
26 blast furnace slag (GBFS) pastes after one year of exposure in the natural laboratory
27 conditions. The chemical changes due to carbonation were examined by X-ray diffraction
28 (XRD), scanning electron microscope/energy-dispersive X-ray (SEM-EDX) and attenuated
29 total reflectance Fourier transformed infrared spectroscopy (ATR-FTIR). Subsequently, the
30 pore structure and E_m of the degraded material were tested by mercury intrusion porosimetry
31 (MIP), nitrogen (N_2) adsorption, and nanoindentation.

1 The chemical degradation of alkali-activated pastes due to natural carbonation is
2 showed to be dependent on the GBFS content and their pore structure development. It was
3 found that the pure alkali-activated GBFS paste was not carbonated at all within the tested
4 period due to fine gel pore structure. On the other hand, carbonation of the gel in the pastes
5 consisting FA and GBFS generated significant mineralogical and microstructural changes.
6 The extensive decalcification of the gel was reflected in the increase of nanoporosity.
7 Consequently, the E_m of the carbonated pastes decreased.

8 This study suggests that the degradation of alkali-activated FA and GBFS pastes due
9 to carbonation may be accurately evaluated through micromechanical properties
10 measurements rather than only by testing alkalinity of the pore solution and corrosion of
11 reinforcement such as commonly studied carbonation effect in the ordinary Portland cement
12 (OPC)-based materials.

13 **Keywords:** Alkali-activated FA/GBFS, Natural carbonation, Pore structure, Nanoindentation,
14 E_m

15

16

17

18

19

20

21

22

23

1 **1. Introduction**

2 Alkali-activated materials (AAM), as environmentally friendly alternatives to OPC-
3 based materials due to their comparatively low CO₂ emission and low natural resources
4 consumption, have received much attention in the last twenty years [1, 2]. AAM can be
5 produced from mixing different industrial by-products, such as FA, GBFS, bottom ash, waste
6 glass, agricultural waste etc. with appropriate alkaline solutions [3]. In comparison with OPC-
7 based materials, AAM might have better mechanical properties, stronger interfacial transition
8 zone (ITZ), and better fire and chemical resistance [4]. However, the long-term properties of
9 AAM, specifically carbonation resistance, are still unknown, which limits their application in
10 engineering practice [5, 6].

11 In general, the CO₂ gas reaction-diffusion process in porous media is controlled by
12 both the concentration gradient of CO₂ and the rate of the chemical reaction. Carbonation rate
13 and degree in OPC-based materials and AAM depends on their physical and chemical
14 properties and exposure conditions (i.e. relative humidity (RH), CO₂ concentration,
15 temperature, duration of exposure). However, OPC-based materials and AAM exhibits
16 different mechanisms during carbonation [7-10], due to formation and interaction of different
17 phases in these two systems. While portlandite (Ca(OH)₂) and calcium silicate hydrate gel (C-
18 S-H) are the primary sources of Ca²⁺ ions in the carbonation process of OPC-based materials
19 [11], the alkali calcium aluminate silicate hydrate gel, denoted further in the text as a C-(N-
20)A-S-H gel, similar to [12], is the main source of Ca²⁺ ions for carbonation reactions in
21 GBFS-based or different blended AAM (GBFS, FA, metakaolin). The removal of the calcium
22 ions from the gel interlayers and gel sheet layers during carbonation induces shrinkage due to
23 the molecular structural reorganization of the gels. This reaction is followed by a decrease in
24 the volume of the paste, which is called carbonation shrinkage [13].

1 Depending on the binder composition, the effect of carbonation on the mechanical
2 properties can vary. Mechanical properties of OPC pastes can be considerably improved by
3 carbonation [14, 15], because carbonation of the $\text{Ca}(\text{OH})_2$ leads to a reduction in porosity due
4 to the positive difference of molar volumes between $\text{Ca}(\text{OH})_2$ and CaCO_3 . Measured by
5 nanoindentation, hardness and elastic modulus tend to shift to higher values in the OPC paste.
6 On the other hand, micro-mechanical properties of blended OPC and GBFS (such as CEM III-
7 B) pastes decrease due to carbonation, since they contain less $\text{Ca}(\text{OH})_2$ and have a lower
8 Ca/Si ratio in the C-S-H gel [16, 17]. It has been found that at extensive levels of
9 decalcification (when Ca/Si is below ~ 0.66), decomposition of the Ca-O sheets of the C-S-H
10 leads to significant shrinkage due to precipitation of calcium carbonates and subsequent
11 polymerization of the silica gel [18], resulting in decrease of the mechanical strength.

12 Only a few studies so far have discussed mechanical behavior of carbonated AAM.
13 For instance, Bakharev et al. [7] found that the carbonation resistance of alkali-activated slag
14 (AAS) concrete was lower than that of OPC concrete. The AAS concrete had higher strength
15 loss and carbonation depth than OPC concrete in both investigated exposure conditions, i.e.
16 immersion in 0.352 molar (M) sodium bicarbonate solution, and exposure to atmosphere with
17 10–20% of CO_2 at 70% RH. Nevertheless, both sets of the conditions are highly aggressive
18 and the results cannot be directly used to predict in-service behavior of AAS concrete
19 subjected to natural carbonation.

20 Bernal et al. investigated accelerated carbonation of alkali silicate-activated GBFS
21 mortars, under the condition of CO_2 concentration of $3.0 \pm 0.2\%$, temperature of 20 ± 2 °C, and
22 $65 \pm 5\%$ RH [19]. Noncarbonated specimens had compressive strengths of up to 63 MPa after
23 28 days of curing when granulated GBFS was used as the sole binder. The strength decreased
24 by 40-50% after carbonation.

1 Puertas et al. [9] studied the effect of alkaline activator on carbonation degree in AAS
2 mortars in terms of mechanical properties. When sodium waterglass was used as an activator,
3 decalcification of the C-S-H gel prompted by carbonation led to a loss of cohesion in the
4 matrix, increase in porosity, and the reduction of the compressive strength. On the other hand,
5 when NaOH was used as activator, carbonation enhanced the compressive strength of the
6 mortar. The authors assumed that this was due to the precipitation of calcium carbonates in
7 the pores, causing a decline in the total porosity and average pore size.

8 Since effect of carbonation in the previous studies was mainly investigated on bulk
9 macro-mechanical properties of alkali-activated mortars or concretes, it is difficult to
10 understand its effects on the local micro-mechanical properties of the binder. Several
11 parameters can affect the interpretation of the mechanical behavior of the material due to the
12 carbonation if they are studied at concrete (macro) level and not at the paste (micro) level.
13 The most important are:

- 14 • Effect of the material scale: Pastes are more suitable for the analysis due to their
15 homogeneity, compared to concrete. The presence of aggregates in the concrete
16 encompasses paste aggregate interface, which can carbonate faster due to its higher
17 porosity compared to the paste itself. Therefore, the carbonation study on the paste
18 samples is needed first for understanding of more complex carbonation mechanism at
19 the concrete scale.
- 20 • Effect of the sample size: Carbonation reaction is dominant at the concrete surface
21 and in the first several millimeter depth from the surface. Therefore, effects of
22 measuring the bulk mechanical properties (compressive, tensile or flexural strength)
23 will be largely dependent on the size of the sample. For instance, the standard
24 150x150x150 mm³ concrete cubes NEN [5988:1999] will be useless in evaluation of
25 the natural carbonation effect on the compressive strength if the carbonated depth is

1 only a few millimeter. On the other hand, the coupled effects of different mechanisms
2 at the concrete surface (e.g. drying shrinkage that can lead to cracking) and not only
3 carbonation can overestimate the effect of the carbonation on the material properties.

- 4 • Effect of the testing scale (local/bulk): Testing of the local micromechanical properties
5 provides a more reliable evaluation on chemical degradation of the paste, compared to
6 a bulk test such as the compressive strength test of a standard concrete cube. With a
7 local analysis the chemical degradation of the different phases present in the system
8 can be distinguished and correlated with the chemical analysis. Furthermore, on the
9 same sample, testing of both, carbonated and noncarbonated areas is possible.

10 Considering these effects, it is clear that understanding the influence of carbonation on
11 the micro-mechanical properties at the paste level is the first step towards understanding the
12 properties of carbonated concrete. Therefore, assessment of the micro-mechanical properties
13 is needed, such as E_m , which might be of great importance for predicting the service life and
14 degradation degree of AAM.

15 The aim of this study was to evaluate the effect of chemical changes in the alkali-
16 activated FA and GBFS pastes when exposed in the natural laboratory conditions (~55% RH,
17 ~0.038% CO₂ v/v) on the pore structure and E_m . The gel structural changes were investigated
18 by XRD, SEM-EDX and ATR-FTIR, while MIP, N₂ adsorption, and nanoindentation were
19 used to examine pore structure and E_m after carbonation.

20 **2. Materials and methods**

21 2.1. Materials and sample preparation

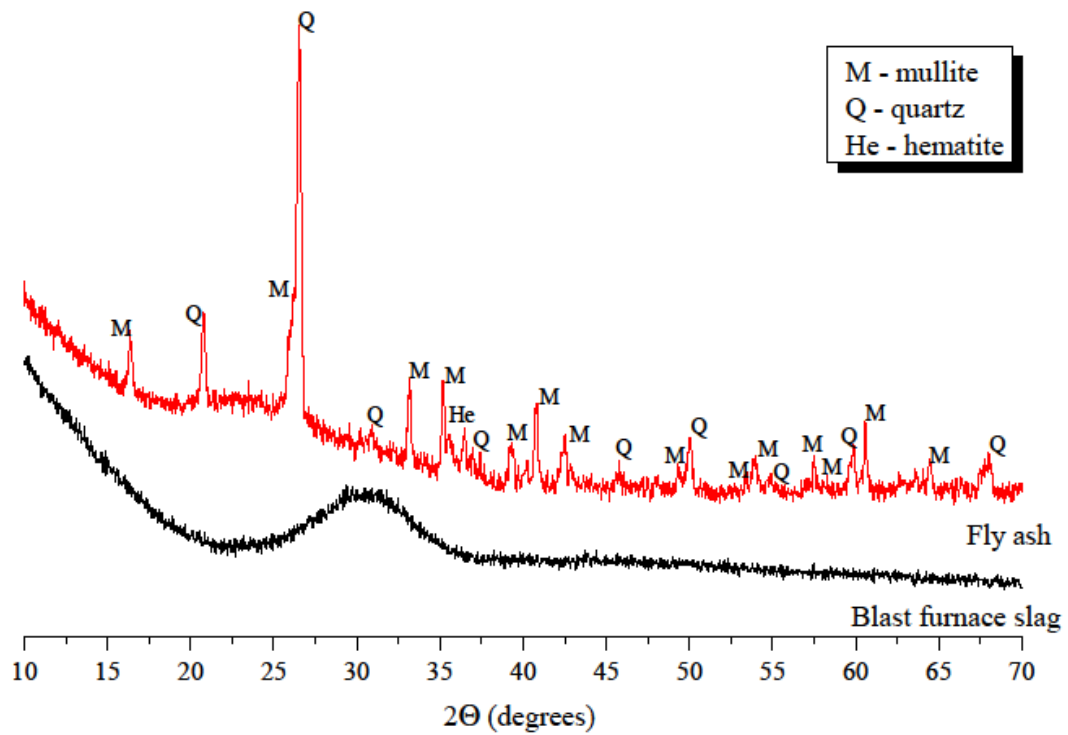
22 The precursors used in this study were FA from VLIEGASUNIE BV and GBFS from
23 ORCEM (the Netherlands), with chemical compositions as shown in Table 1. The main
24 crystalline phases in FA were quartz, mullite, and hematite, while GBFS was mainly

1 amorphous, as showed by XRD scans (Fig. 1). The alkaline activator was synthesized by
2 mixing anhydrous pellets of sodium hydroxide with deionized water and commercial sodium
3 silicate solution (27.5 wt.% SiO₂, 8.25 wt.% Na₂O). The activator concentration was 4.8 wt.%
4 Na₂O with respect to the mass of precursor (FA + GBFS). After mixing, the activator was
5 kept in the laboratory with temperature around 20°C to cool down for 24 h prior to the
6 preparation of the pastes. For each paste, the liquid to binder mass ratio was 0.5. Pastes were
7 produced with the following FA/GBFS ratios: 100:0, 70:30, 50:50, 30:70, 0:100 wt.%, named
8 S0, S30, S50, S70, S100, respectively. The precursors were dry-mixed for 2 minutes and then
9 mixed with the activator. The pastes exposed to carbonation were cast in cylinders with 54
10 mm diameter and height of 100 mm. The samples were placed in a fog room with 20°C and
11 99 % RH and cured under sealed conditions for 28 days. After 28 days, the samples were
12 demolded and exposed in the indoor laboratory conditions at 20°C and 55 % RH,
13 CO₂~0.038% v/v for 1 year. In addition, reference samples were kept in sealed conditions (i.e.
14 without CO₂) until the characterization was carried out. The representative samples prior to
15 microscopic examination are shown in Fig. 2. The carbonation depth was determined by
16 polarized light microscope (PLM) under cross polarized light as demonstrated in previous
17 study [20]. The carbonation depth values are presented in the Fig. 3.

18 **Table 1**

19 Chemical compositions of FA and GBFS measured by X-ray fluorescence.

	SiO ₂	Al ₂ O ₃	CaO	MgO	Fe ₂ O ₃	SO ₃	Na ₂ O	K ₂ O	TiO ₂	P ₂ O ₅	L.O.I.
FA	54.28	23.32	4.23	1.62	8.01	0.64	0.85	1.97	1.23	0.54	3.37
GBFS	34.40	11.53	39.17	7.81	1.42	1.6	0.23	0.58	-	-	1.15



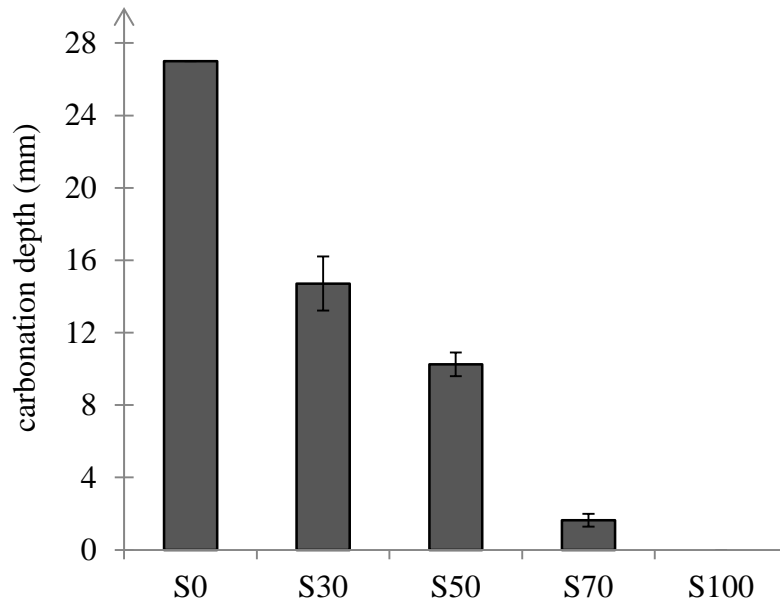
1

2 **Fig. 1.** XRD scans of original FA and GBFS.



3

4 **Fig. 2.** Cross-sections of representative samples after natural laboratory carbonation of 1 year,
 5 clearly showing the outer (carbonated) and the inner (noncarbonated) zone. Reference
 6 samples are of smaller diameter, placed beneath the exposed samples.



1

2 **Fig. 3.** Carbonation depth after 1 year exposure in the natural laboratory conditions,
 3 determined by PLM in the alkali-activated pastes as a function of the slag content.

4 2.2. Test methods

5 2.2.1 XRD

6

7 For XRD phase identification, the representative samples after 1 year of curing, and 1
 8 year of exposure were gently crushed and then immersed in isopropanol for one week, by
 9 which water is first replaced and then evaporated. Subsequently, samples were placed under
 10 vacuum at 25 °C for minimum three weeks. In order to calculate the absolute phase weight
 11 proportions, the standard was homogeneously mixed with the sample. A few grams of
 12 hydration-stopped samples, were ground in a McCrone micronizing mill to below 15 μm,
 13 with an internal standard. The known amount (10 wt.%) of internal standard which in this
 14 study was silicon (Si) has been used. XRD scans were acquired from 5° to 70° 2-theta with a
 15 Bruker D4 diffractometer using Co-Kα radiation and a Vantec detector. The identified phases
 16 were added to the Rietveld refinement. The software package Topas was used to perform
 17 Rietveld quantification of phases in the reference and exposed samples. Regarding precision

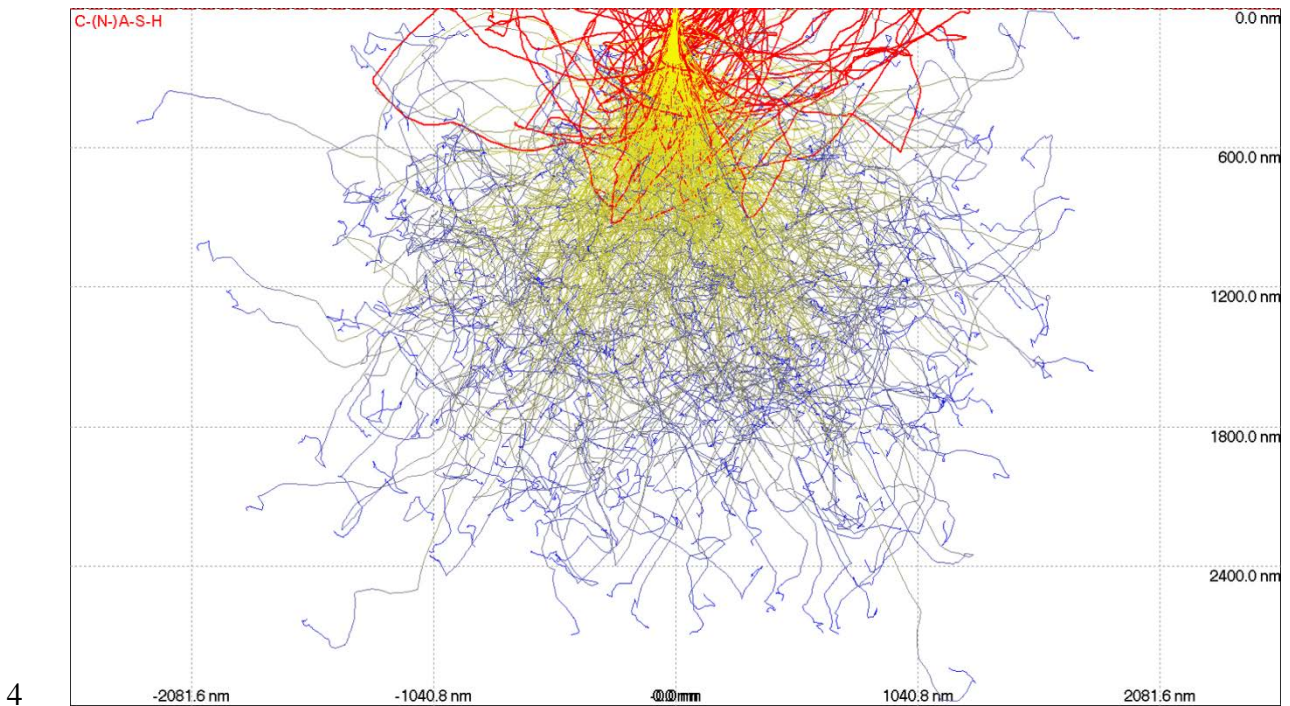
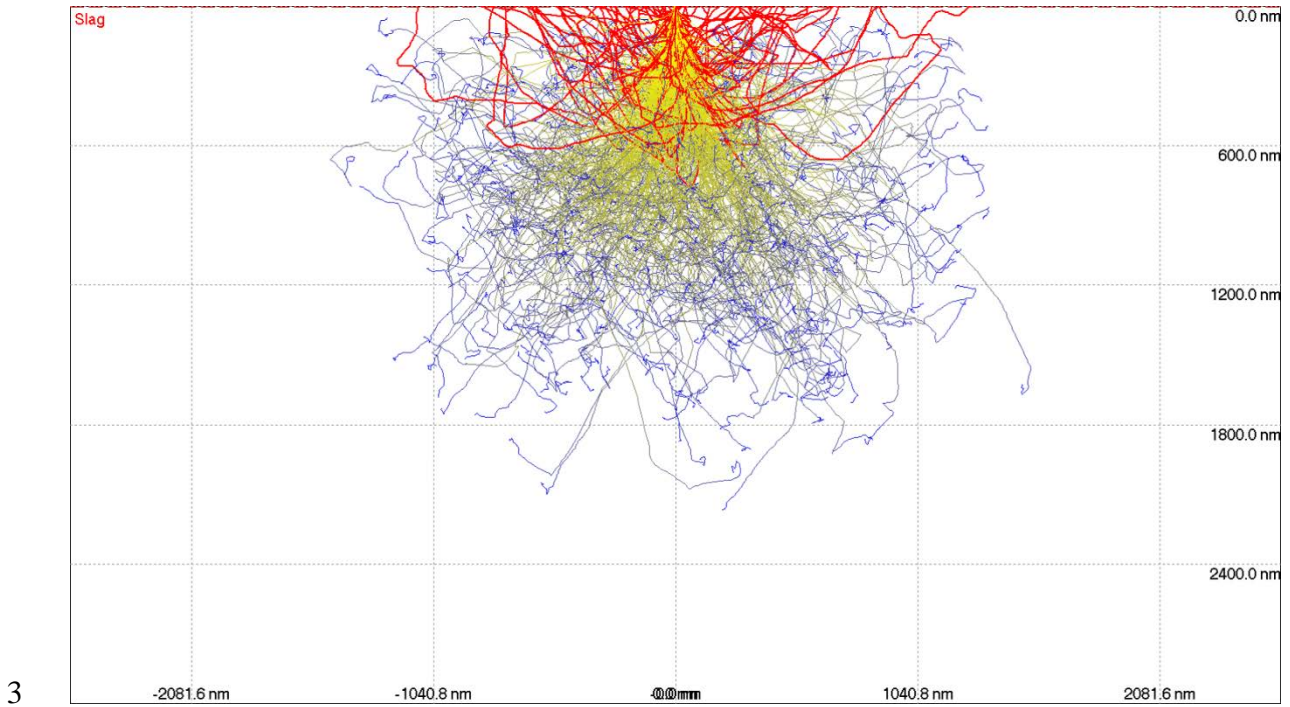
1 obtained on the content of the amorphous phase in the samples, the calculation showed high-
2 precision results, with errors generally less than 1.0% absolute.

3 2.2.2 SEM-EDX 4

5 For SEM-EDX sample preparation, the hydration of the samples was stopped in the
6 same way as for XRD analysis, whereas instead of grinding the samples into a powder, the
7 reference and exposed samples (crushed into small pieces with dimensions of 1-2 cm³) were
8 impregnated using a low viscosity epoxy resin and polished down to ¼ µm.

9 To study the microstructure a Philips-XL30-ESEM was used, equipped with NSS.3.3
10 software. This instrument was used in normal high-vacuum mode as a regular SEM. In order
11 to determine optimal microscope condition for microstructure analysis, the interaction volume
12 was modelled using Monte Carlo simulation in Casino v2.41 software
13 (www.gel.usherbrooke.ca/casino/index.html) for unreacted GBFS and for the C-(N-)A-S-H
14 gel that is formed in alkali-activated GBFS [12] (Fig. 4), using their experimental density (
15 2.9 g/cm³ for GBFS and 2.6 g/cm³ C-(N-)A-S-H gel) as an input parameter. First, the multiple
16 energies were simulated (not shown here) from 5 to 20 kV with a step of 5, in order to
17 demonstrate the effect of the accelerated voltage on the depth and the width of the electrons-
18 solid material interaction. Fig. 4 demonstrates the depth of the electrons-solid material
19 interaction, while using 15 kV for the simulation, which was chosen as an optimum in this
20 study for experiments from previous iterative study. It was found that the maximum
21 penetration depth of the electron trajectories ranges from 0.6 to 1.8 µm for GBFS particles
22 and from 1.0 to 2.5 µm for C-(N-)A-S-H gel at 15 kV (Fig. 4). For backscattered electrons,
23 the maximum sampling depth is about 30% of the interaction volume depth and its lateral
24 dimension is close to the interaction volume depth. As electrons penetrate deeper, the lateral

1 spread of the electron-solid interaction region increases. The lateral dimension of the
2 interaction volume for cement-based materials is thought to be around 1-2 μm [21].



5 **Fig. 4.** Monte Carlo simulation of the penetration of 1000 electrons accelerated at 15kV in a
6 beam of radius 10 nm into a GBFS (upper image) and C-(N-)A-S-H gel (bottom image). (The
7 red trajectories are back-scattered electrons, which result from elastic scattering events.

1 Inelastic scattering events cause a reduction of energy of the electrons until eventual
2 disappearance in the specimen bulk. Yellow trajectories represents high energy and blue
3 represents low energy trajectories.)

4 For chemical compositions of the reaction products, SEM-EDX point analyses were used.
5 Carbon coating was applied to the polished sections of the samples. Approximately 30 points
6 were captured and analysed in each carbonated and noncarbonated gel area per sample. The
7 mean atomic ratios for Na/Si, Mg/Si, Ca/Si, Al/Si were then obtained by averaging the values
8 from more than 30 points. The points were chosen combining SEM-EDX at magnification
9 sufficient to resolve carbonation features. Before and after each spot measurement,
10 corrections were applied using ZAF method. The ZAF method is aimed to convert apparent
11 concentrations (raw peak intensity) into (semi-quantitative) concentrations corrected for inter-
12 element matrix effects. The ZAF method is iterative and in order to proceed it needs
13 information on concentrations. However, these are absent at the beginning. Thus the results
14 from the first iteration are fed back to the second and so on until a limit is reached that is
15 statistically satisfactory.

16 2.2.3 ATR-FTIR

17

18 The chemical bonds of the powdered reference and carbonated samples were
19 characterized by ATR-FTIR. Spectra were acquired using PerkinElmer Spectrum 100, over
20 the wavelength range of 2000 cm^{-1} to 600 cm^{-1} with a resolution of 4 cm^{-1} . In total, 16 scans
21 were collected per measurement. Samples were prepared in the same manner as for XRD
22 measurements.

23 2.2.4 MIP and N_2

24

1 Porosity and pore-size distribution were investigated by MIP measurements combined
2 with N₂ adsorption, following the sample preparation procedure as described for XRD
3 analysis, with exception that samples were not ground. MIP measurements were performed
4 with Micrometrics PoreSizer[®] 9320. The PoreSizer[®] 9320 is a 207-MPa mercury intrusion
5 porosimeter, which determines pore sizes in the range of 7 nm to 500 μm. The threshold pore
6 size was obtained from the intersection of the two tangents in the intrusion curve, such as
7 showed in [21], using Washburn's equation, with a contact angle of 140° and a surface tension
8 of 0.485 N/m [22]. The pore size distribution in the range of 2-37 nm were determined by N₂
9 adsorption. The N₂ adsorption tests were conducted by using Gemini VII 2390 with a relative
10 pressure (P/P₀) range from 0.05~0.99 (the relative pressure is defined as the equilibrium vapor
11 pressure divided by the saturation vapor pressure). Approximately 1 gram of sample was used
12 for the analysis. According to N₂ adsorption isotherm the pore volume and area distribution
13 were calculated by the Barrett-Joyner-Halenda (BJH) method [23]. The sharp peaks that were
14 found in the pore size distributions curves, corresponding to the threshold (critical) pore
15 diameter, were determined according to [24].

16 2.2.5 Nanoindentation

17

18 Nanoindentation is a widely used technique for testing nano or micro-mechanical
19 properties of cementitious materials [25-29], and also of AAM [30-34]. For heterogeneous
20 multiphase materials, a statistical indentation method can be used, by analyzing a large
21 number of indents within a representative sample area [35, 36]. It consists of indenting a
22 sample surface with a diamond indenter, followed by a loading-unloading cycle while
23 continuously recording the load and indentation depth. From the load-displacement slope and
24 calibrated contact area, E_m of the material at the microscale can be determined.

1 Nanoindentation testing was conducted using Agilent Nano Indenter G200, equipped
2 with a Berkovich indenter. Nanoindentation was used to examine E_m , for carbonated and
3 noncarbonated areas. The samples for nanoindentation testing were first cut into slices of
4 approximately 10 mm thickness. Then they were ground and polished following the procedure
5 described in Table 2, to obtain a very flat and smooth (“mirror-like”) surface. The tests were
6 set in such a way that the loading was applied when the indenter comes into the contact with
7 the surface of the sample until a specified maximum penetration depth is reached. Afterwards,
8 the load was maintained for 10 seconds followed by the unloading cycle. A typical example
9 of an indentation curve is shown in Fig. 6. The indentation depth was 2000 nm. This depth
10 was chosen because the scale of SEM-EDX analysis was ~2000 nm, which allows the
11 correlation between chemical and micro-mechanical results, as reported by Ulm et al. [37,
12 38].

13 The measurements were performed on the top surface of the specimens. The E_m
14 measurements were obtained from a matrix of 15x15 indents, with a distance of 40 μm
15 between individual indents. The indentation mesh for the noncarbonated S50 sample is
16 visualized in Fig. 5.

17 The Continuous Stiffness Method developed by Oliver and Pharr [39] was used to
18 calculate the reduced modulus of elasticity (E_r), according to Eq. (1):

$$E_r = \frac{\sqrt{\pi}}{2} \frac{S}{\sqrt{A_c}} \quad (1)$$

19 where S is the contact stiffness determined from the load-indentation depth slope, and A_c is
20 the contact area under load (μm^2), which is the function of the indentation depth. Since the
21 effect of non-rigid indenter also must be taken in account, the modulus of elasticity of the
22 sample, E_s (GPa) is calculated from the Eq. (2):

$$\frac{1}{E_r} = \frac{(1 - \nu_s)^2}{E_s} + \frac{(1 - \nu_i)^2}{E_i} \quad (2)$$

1 where ν_s is the Poisson's ratio of the sample, which was assumed to be 0.18 for all
 2 measurements. E_i is the modulus of elasticity of the diamond indenter, and ν_i is the Poisson's
 3 ratio of the diamond indenter ($E_i = 1141$ GPa, $\nu_i = 0.07$).

4 This method enables that E_m is obtained as a continuous function of the indentation depth.
 5 Therefore, for each indent, the average E_m was determined in the loading range between 1000
 6 and 1800 nm depth.

7

8 **Table 2**

9 Polishing procedure of the samples adopted in this study for SEM-EDX and Nanoindentation
 10 measurements.

Sandpaper	Grit (μm)	Methods	Duration (min)
P-grade 120	125	With ethanol	5
P-grade 320	46.2	With ethanol	5
P-grade 500	30.2	With ethanol	5
P-grade 800	25.8	With ethanol	5
P-grade 1200	15.3	With ethanol	5
Diamond paste	6	Ultrasonic bath with ethanol, air gun dry	5
Diamond paste	3	Ultrasonic bath with ethanol, air gun dry	5
Diamond paste	1	Ultrasonic bath with ethanol, air gun dry	5
Diamond paste	0.25	Ultrasonic bath with ethanol, air gun dry	5

11
12
13
14

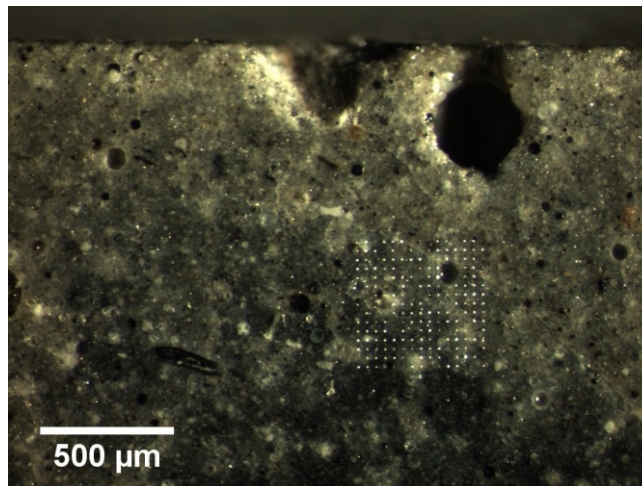


Fig. 5. Light microscope photo of the area of indents in noncarbonated S50 sample.

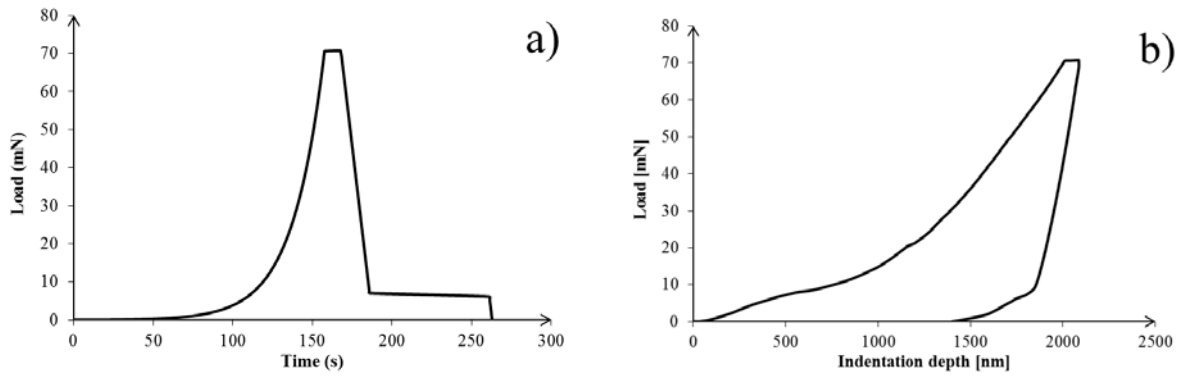


Fig. 6. Example of (a) load-time and (b) load-indentation depth curves by nanoindentation.

1

2 **3. Results and discussion**

3 In this section, results are presented in five subsections. First, the characterization of
 4 the carbonation products is shown using XRD. Next, the spectroscopic analysis of the
 5 carbonated and noncarbonated gel structure is demonstrated by SEM-EDX and ATR-FTIR.
 6 Subsequently, the pore structure measurements of the carbonated and noncarbonated paste are
 7 discussed. The last subsection shows the effect of carbonation on the elastic modulus, which
 8 was significantly affected by the GBFS content.

9 **3.1. Mineralogical alteration by XRD**

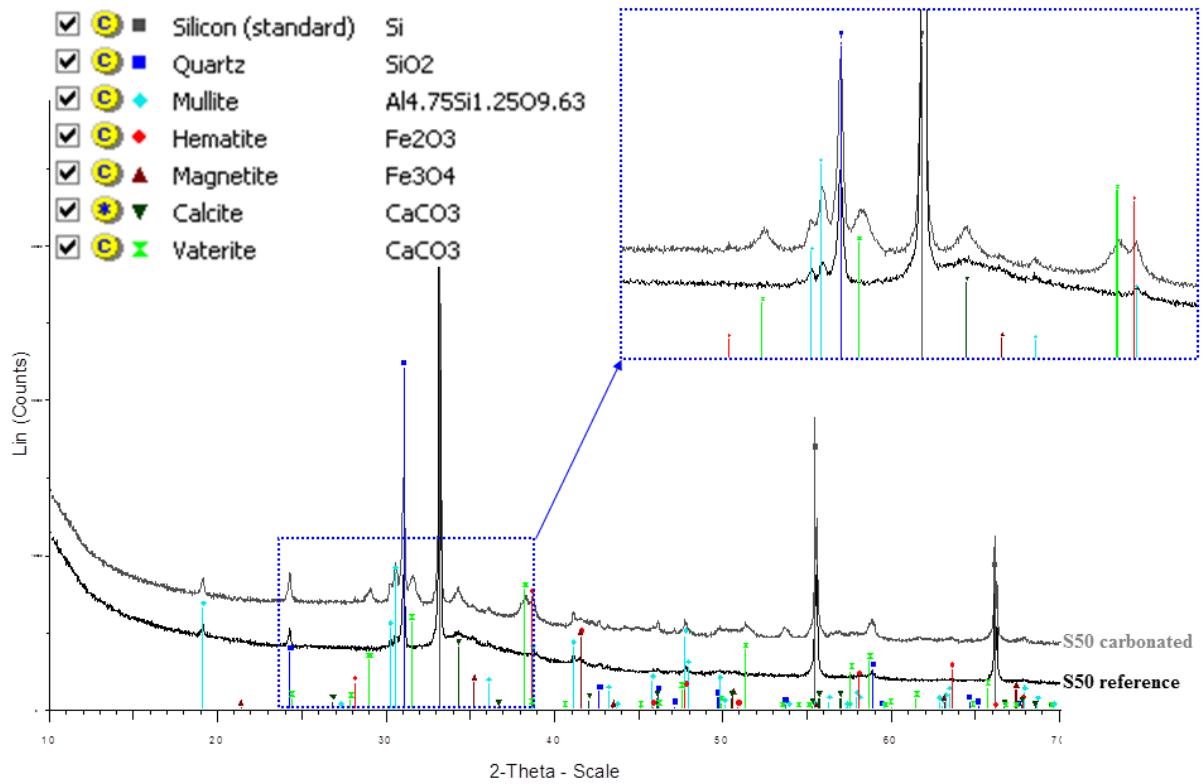
10 The aim of XRD analysis was to clearly differentiate carbonation products. Fig. 7
 11 shows an example of the qualitative analysis of the reference and carbonated S50 samples.
 12 The major phases for reference S50 sample, were amorphous phase (consisted of unreacted
 13 amorphous phase and reaction phases, i.e. amorphous gel), and crystalline phases such as
 14 quartz (SiO_2), mullite ($\text{Al}_{4.75}\text{Si}_{1.25}\text{O}_{9.63}$), hematite (Fe_2O_3), magnetite (Fe_3O_4), and traces of
 15 calcite (CaCO_3). The identified crystalline phases stem from the original mineralogical
 16 composition of FA. The presence of amorphous phases in Fig. 7 can be recognized by the
 17 broad hump beneath the diffraction peaks of the crystalline phases centred around $34^\circ 2\theta$
 18 (detailed offset made patterns visible in the same graph, Fig 7). The amorphous phase content
 19 decreased for carbonated S50 sample, compared to the reference S50 sample (Fig. 8).

1 Carbonation of the reaction products in S50 paste has resulted in the formation of vaterite and
2 calcite. The same carbonation products were identified for S30 and S70 exposed samples.

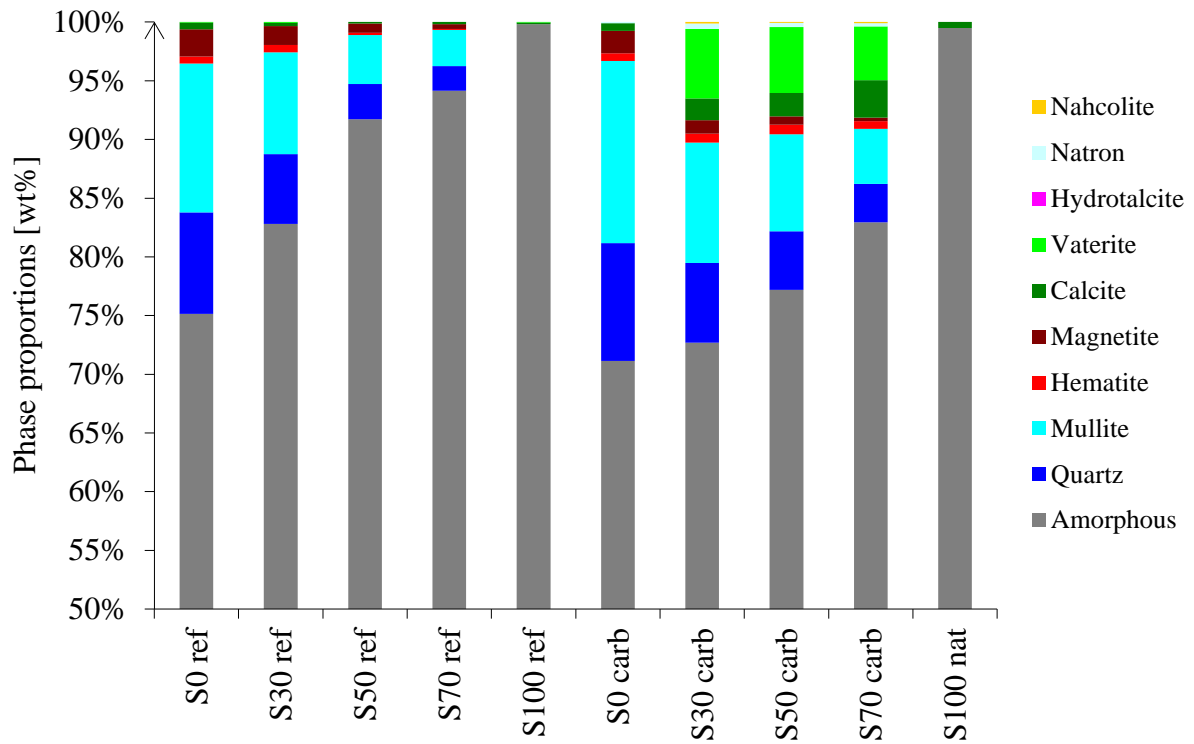
3 The quantitative phase analysis is given in Fig. 8, where the results are normalised to
4 100 %. The major phase in pastes was amorphous (> 70 wt.%) for both, reference and
5 samples exposed in the natural laboratory conditions. The reference samples consisted of FA
6 or FA and GBFS, have similar phases, whereas the amorphous content increased with an
7 increase of GBFS. In the sample S100, no other phases except minor traces of calcite (< 0.5
8 wt.%) were identified for both reference and exposed samples, indicating that reaction
9 products were not carbonated. Similarly, reaction products in sample S0 did not undergo
10 carbonation, such as shown in Section 3.3. However, sodium-based carbonates, natron
11 ($\text{Na}_2\text{CO}_3 \cdot 10\text{H}_2\text{O}$) and nahcolite (NaHCO_3), were identified in the exposed S0 sample, as a
12 products from the carbonation of pore solution. In addition, amorphous phase proportions
13 were found to be different for reference and exposed S0 samples. Higher content of the
14 amorphous phase in the reference S0 sample, was attributed to the curing conditions. The
15 reference samples were kept in the sealed conditions until the testing. No water exchange was
16 possible between the sample and environment, which most likely contributed to higher
17 reaction degree and higher amount of the reaction products in reference S0 sample, compared
18 to the carbonated sample. On the other hand, content of the carbonation products in S30, S50
19 and S70 pastes, were 10.1, 14.5 and 11.2 wt. %, respectively. Rietveld quantification of
20 phases revealed that the proportion of vaterite was dominant (Fig. 8). Vaterite is well known
21 as an unstable precipitate in supersaturated solutions, caused by a nonstoichiometric reaction
22 conditions as showed by Jung et al. [40]. The nucleation of different calcium carbonates is
23 reported to be dependent on the supersaturation level, ionic ratio of $[\text{Ca}^{2+}]/[\text{CO}_2^{3-}]$ in solution
24 and the pH of solution [40-42]. According to Hostomsky et al. [43], precipitation of vaterite in
25 the reaction of calcium nitrate and sodium carbonate occurs at $\text{pH} \geq 9.5$, but calcite is obtained

1 at $\text{pH} \leq 8.5$. In addition, Kralj et al. [42] reported precipitation of pure vaterite from the
2 solution of calcium chloride and sodium carbonate at $9.3 \leq \text{pH} \leq 9.9$. Regarding carbonation as
3 a continuous process followed by a pH decrease, the unstable vaterite might re-crystallize into
4 stable calcite if there is a sufficient moisture [44]. The re-crystallization of vaterite in this
5 study was not the case and it was most probably inhibited by the moisture content (55% RH),
6 but also due to the pH level of the pore solution. The pH of pore solution in AAM after
7 carbonation is generally maintained above 9 due to high carbonate/bicarbonate ratios as
8 showed by Bernal et al. [45] in the natural carbonation conditions, which were the conditions
9 studied in this paper.

10 In contrast to vaterite and to less extent calcite identified in this study, calcite is the
11 main carbonate beside aragonite and vaterite, formed from the natural carbonation of OPC-
12 based paste as found by Hidalgo et al. [46]. Accordingly, the formation of more vaterite than
13 calcite in this study can be partially attributed to the nanostructural ordering and
14 thermodynamic stability of the C-(N)-A-S-H gel in alkali-activated pastes, compared to C-S-
15 H gel in OPC-based pastes. White et al. [47] have investigated intrinsic differences in atomic
16 ordering of calcium (alumino) silicate hydrates in conventional and alkali-activated cements.
17 The authors found large intrinsic differences in the extent of nanoscale ordering between C-
18 S-H derived from C_3S and alkali-activated GBFS systems using X-ray total scattering. It is
19 showed that C-(N-)A-S-H gel is mostly amorphous and intrinsically less thermodynamically
20 stable than (nano)crystalline C_3S -based gels. This implies different phase dissolution
21 mechanism regarding carbonation of AAM compared to OPC-based materials, which results
22 in precipitation of different CaCO_3 polymorphs. In this regard, by comparing the main
23 carbonation products in AAM as from this paper (vaterite) with carbonation products from
24 OPC-based materials [46] (calcite), both from the natural laboratory conditions, it is showed
25 that the previous implication is valid.



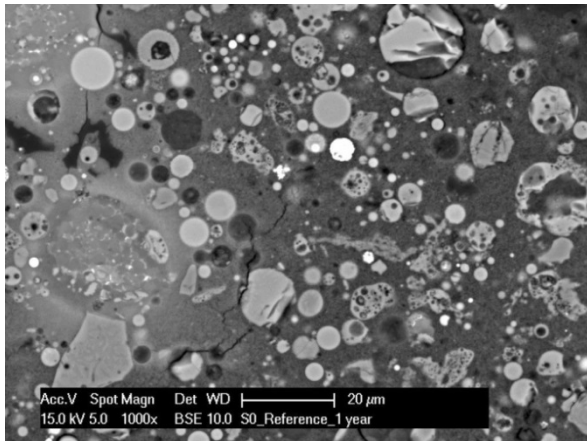
1
2 **Fig. 7.** Comparison of the XRD scans with respect to the phases in reference and carbonated
3 S50 paste.



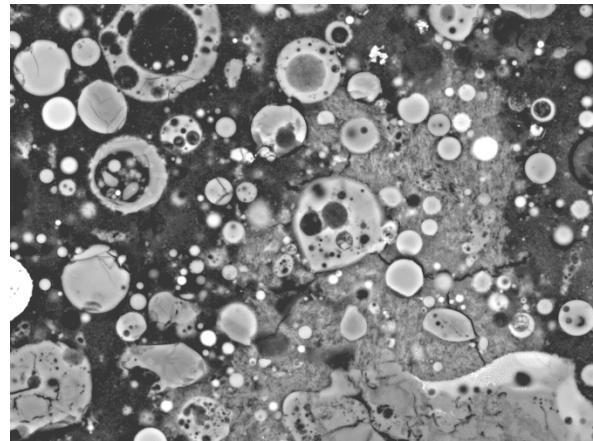
1 **Fig. 8.** Quantitative phase analysis by Rietveld method for reference pastes and for the pastes
2 exposed in the natural laboratory conditions.

3 3.2. Decalcification degree determined by SEM-EDX

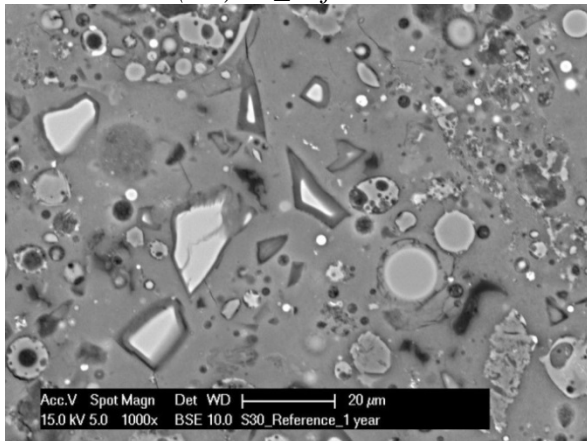
4 Fig. 9 demonstrates the contrast of microstructures between reference pastes and
5 pastes exposed in the natural laboratory conditions. In reference pastes, more uniform and
6 denser microstructure is formed with a higher GBFS content. In the carbonated areas in the
7 samples S30, S50, S70 four main features can be observed (Fig. 9, *b-ii*, *c-ii*, *d-ii*): (1) pores
8 and microcracks, (2) carbonated gel with decrease in average atomic mass, (3) noncarbonated
9 gel isolated from the carbonated part, (4) unreacted FA and GBFS particles. This is in
10 agreement with a previous study of Sisomphon et al. [48], who observed a similar morphology
11 of the carbonated microstructure in GBFS mortars (made by CEM III/B 42,5 N and CEM I
12 42,5 N) after 1 year of carbonation in the natural atmospheric conditions. The difference of
13 gel greyscale levels in backscattered electron (BSE) images between noncarbonated and
14 carbonated areas (Fig. 9, *b-ii*, *c-ii*, *d-ii*), is attributed to their different nanoporosities and
15 therefore to different densities and backscattered electron coefficients, as found by Famy et al.
16 [49]. The samples S0 and S100 were not carbonated, which can be clearly seen when the CO₂
17 exposed microstructures are compared to the corresponding reference microstructures.
18 Therefore, only blended pastes (S30, S50, S70) have been further studied by SEM-EDX for
19 the chemical analysis, since only in these samples the gel was carbonated.



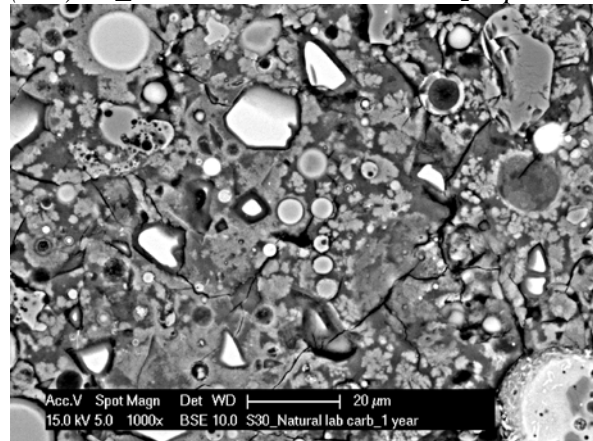
(a-i) S0_reference



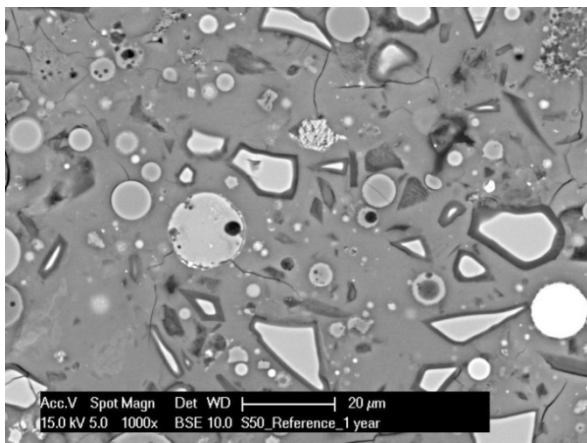
(a-ii) S0_noncarbonated under CO₂ exposure



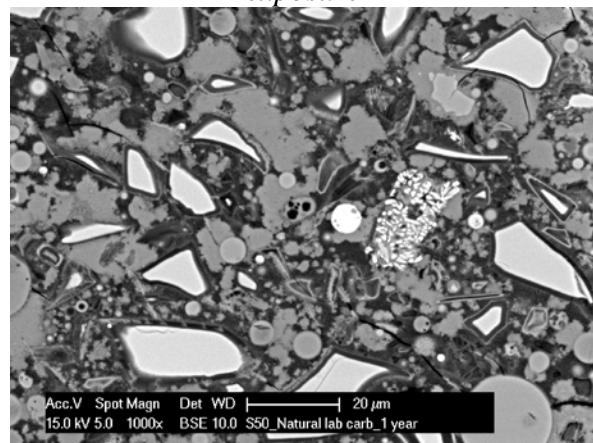
(b-i) S30_reference



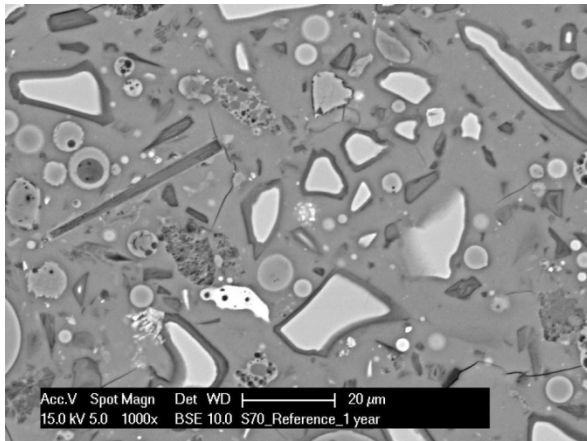
(b-ii) S30_carbonated area under CO₂ exposure



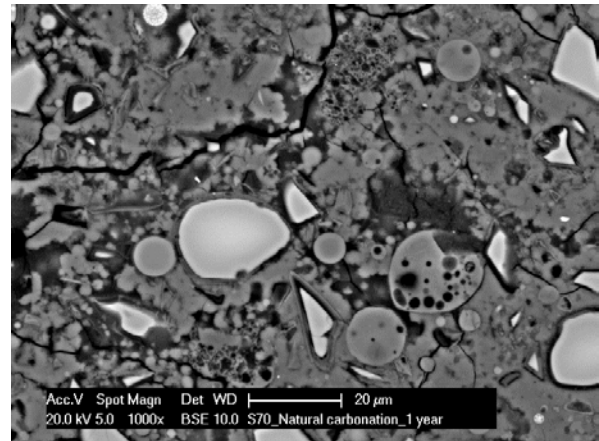
(c-i) S50_reference



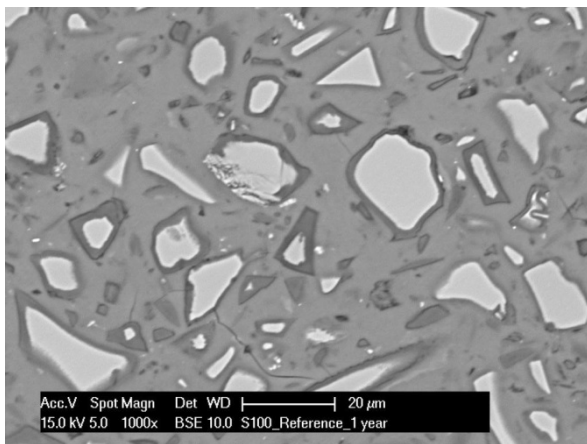
(c-ii) S50_carbonated area under CO₂ exposure



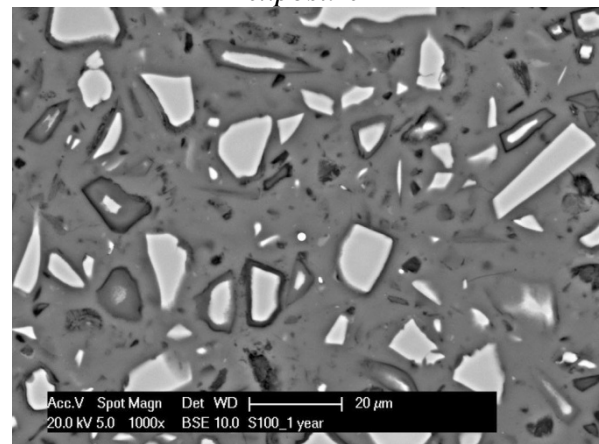
(d-i) S70_reference



(d-ii) S70_carbonated area under CO₂ exposure



(e-i) S100_reference



(e-ii) S100_noncarbonated under CO₂ exposure

1
 2 **Fig. 9.** SEM-BSE images of (i) the microstructures of reference samples, (ii) the
 3 microstructures of samples after 1 year of exposure in the natural laboratory conditions.

4
 5 The EDX spot analyses were made for carbonated and noncarbonated areas (Fig. 9, b-
 6 ii, c-ii, d-ii). In order to study the elemental composition, parameters for consideration
 7 regarding the chemical changes are firstly discussed. The primary carbonation reaction is a
 8 sample surface reaction between dissolved CO₂ gas and pore water. When the dissolved CO₂
 9 molecules diffuse into the material, the pH of the pore solution decreases due to the formation
 10 of carbonic acid. When the pH decreases to 12, the equilibrium between pore solution and the
 11 reaction products is disturbed and the weakest bounded elements will be decomposed from
 12 the gel structure. The Ca²⁺ ions are the first to be decomposed and migrated into the pore

1 solution. The saturation of the pore solution with Ca^{2+} ions and with salts of the carbonic acid
2 will eventually result in calcium carbonates precipitation [50]. The carbonation reaction
3 degree will be limited by the gel solubility, calcium content, the bulk pore volume and ion
4 concentration in the pore solution. If the carbonated pore solution is saturated with Ca^{2+} ions,
5 the gel will be preserved from further decomposition. This can be due to reduced pore volume
6 or high Ca content in the precursor. For instance, paste S100 has the lowest porosity (~3.68%)
7 amongst the tested pastes, as shown in Table 3, suggesting the lowest amount of the pore
8 solution. In addition, this paste has the highest Ca content (Table 3), but its microstructure is
9 not carbonated at all. Therefore, in such a dense system, the pore structure will be governing
10 factor and, irrespectively of the binder chemistry, will limit the carbonation degree. On the
11 contrary, paste S0 has the lowest Ca content and the largest porosity which enables CO_2
12 molecules to diffuse faster and dissolve in the pore solution of this sample. Moreover, it is
13 reported that the gel in alkali-activated FA cannot be carbonated [51], and that carbonation of
14 alkali-activated FA is mainly limited to the pore solution. Therefore, both chemistry and pore
15 structure of the individual systems need to be considered when carbonation degree is to be
16 determined.

17 **Table 3**

18 Summary of the important pastes properties for understanding the carbonation mechanism.

Mixture	pH of the pore solution at 28 days [52]	Ca-content from FA and GBFS (by mass weight), determined by XRF	Critical pore diameter at 28 days (nm), determined by MIP or N ₂ [52]	Porosity at 28 days (percentage of the bulk volume, MIP) [52]
S0	13.45	4.8	110 (MIP)	37.06
S30	13.48	15.30	30 (N ₂ adsorption)	14.87
S50	13.76	22.30	4 (N ₂ adsorption)	7.48
S70	13.83	29.3	4 (N ₂ adsorption)	6.65
S100	13.97	39.8	6 (N ₂ adsorption)	3.68

1 The atomic ratios for the primary elements in the noncarbonated and carbonated areas are
2 given in Table 4. The areas were tested in such a way that the unreacted FA and GBFS
3 particles, or the rims between single particle and the surrounding matrix were excluded from
4 the EDX spot analyses. However, due to possible cross-contamination of the EDX spectra, the
5 lowest atomic ratios indicated by the extremity of the data cluster are reported in Table 4.
6 Regardless of the GBFS content in this study, the Na/Si ratio in the carbonated gel did not
7 change significantly compared to the noncarbonated gel (Fig. 10). The Na/Si ratio for S50 and
8 S70 is higher than for the S30 sample. In pastes with 50 wt.% or more GBFS, it is assumed
9 that the reaction is more intense and more reaction products are formed, consequently
10 absorbing more Na ions in their molecular structures. The Mg/Si ratio showed significant
11 variations in the distribution for S50 and S70 samples compared to the sample S30. The S30
12 sample has the same Mg/Si ratio for both measured areas, i.e. carbonated and noncarbonated,
13 because its composition consisted of only 30 wt.% of GBFS and the results suggest that Mg
14 has not formed other reaction products except being distributed in the gel. The results of
15 Mg/Si ratio for S50 and S70 pastes suggest that the Mg is sporadically distributed throughout
16 the gel and that some other reaction products consisting Mg, such as hydrotalcite showed by
17 Haha et al. [53], are intermixed with the gel, causing the data scattering.

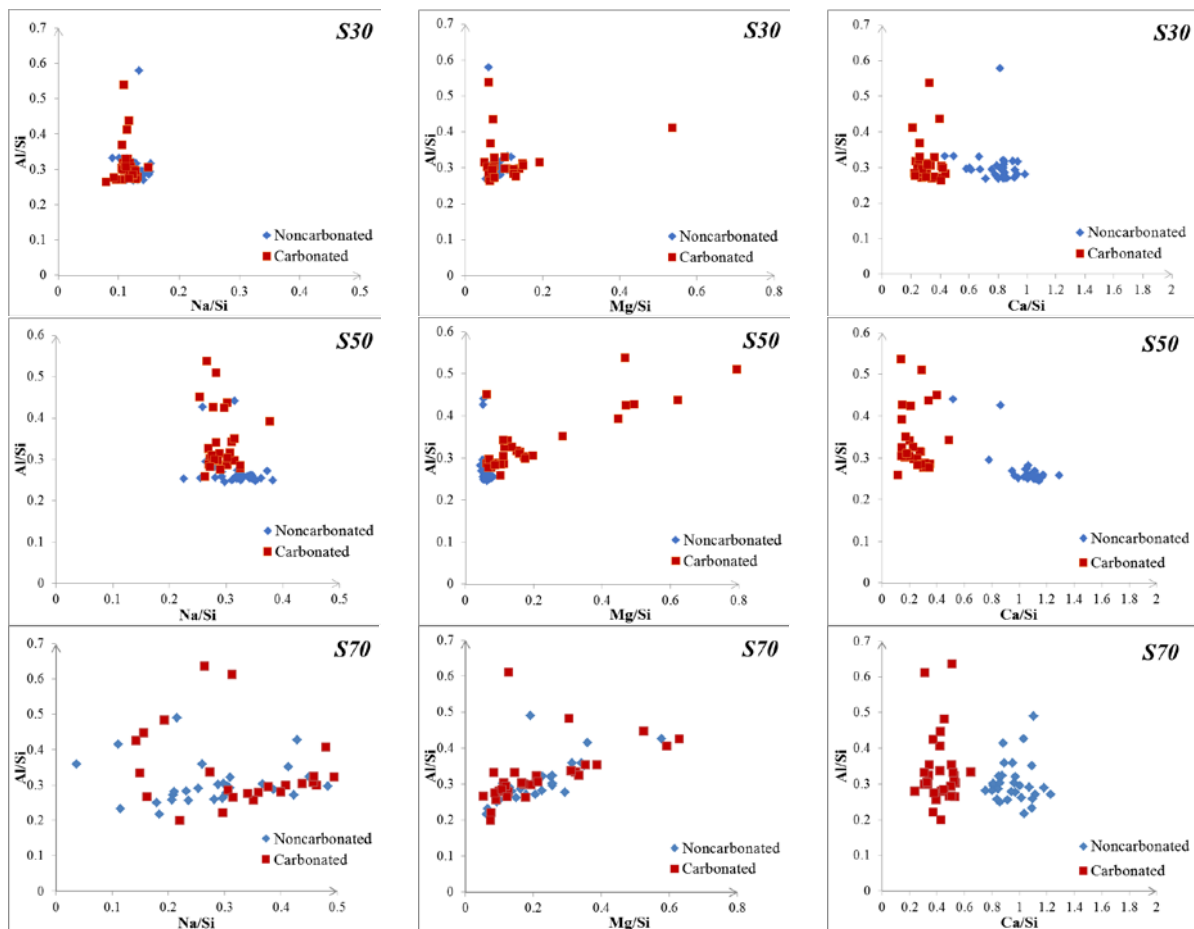
18 Marked decalcification (the last column in Table 4) had occurred in all blended pastes.
19 The Ca/Si ratio has been reduced for the carbonated areas compared to the noncarbonated
20 areas, but the gel was not completely decalcified. Instead, carbonation lowered the Ca/Si ratio
21 until a certain value, which is the lowest for sample S50. Although it was expected that S70
22 sample has a higher decalcification degree since it has a higher Ca amount than S50, the
23 findings show that the decalcification degree was lower. This is most likely due to the finer
24 pore structure of S70 sample compared to S50 sample, which hinders the CO₂ diffusion.

25 **Table 4**

1 Atomic ratios determined for the two areas of the samples by EDX analyses.

Sample	EDX area	Na/Si	Mg/Si	Ca/Si
S30	noncarbonated	0.1	0.05	0.7
	carbonated	0.1	0.05	0.2
S50	noncarbonated	0.25	0.03	0.9
	carbonated	0.25	0.03	0.1
S70	noncarbonated	-	0.07	0.8
	carbonated	-	0.07	0.2

2



3
4 **Fig. 10.** The 2D scatter plots of EDX point analyses with different element atomic ratios in
5 the carbonated and noncarbonated areas of the samples that were exposed in the natural
6 laboratory conditions.

7 3.3. Polymerization degree determined by ATR-FTIR

8 The polymerization of the remaining hydrous silica gel after gel decalcification is
9 demonstrated in the Fig. 11. ATR-FTIR can provide valuable information on the chemical

1 bonds of the silicates in the amorphous material, which is difficult to be studied by XRD. The
2 Si-O stretching modes for the SiQ^n units show infrared absorption bands localized around
3 1100, 1000, 950, 900, and 850 cm^{-1} for $n = 4, 3, 2, 1,$ and 0, respectively [54]. These values
4 shift to higher wavenumbers when degree of silicon polymerization increases, such as found
5 in the carbonated phases of cementitious materials [18]. In this study, ATR-FTIR
6 measurements are used to identify new bands corresponding to carbonation products and to
7 observe the change of the primary silicate bands. The analysis was based on comparison
8 between reference and carbonated samples of alkali-activated pastes.

9 The infrared spectra of the unreacted FA and GBFS pastes are shown in Fig. 11, in the
10 spectra of samples S0 and S100 (red lines). The main band for unreacted FA is found at 1046
11 cm^{-1} , which is assigned to Si-O-T bands, while weaker bands were identified at 798, 780, and
12 695 cm^{-1} indicating the presence of quartz [55]. On the other hand, the unreacted GBFS shows
13 the main vibration band located at 905 cm^{-1} , which is due to the asymmetric stretching
14 vibration of terminal Si-O bands. The evolution of the spectrum when FA was activated is
15 mainly seen as a shift of the stretching band (1046 cm^{-1} for unreacted FA), to lower
16 wavenumber (980 cm^{-1} for alkali-activated FA), while for alkali-activated GBFS a shift of the
17 stretching band (905 cm^{-1} for unreacted GBFS) was to higher wavenumber (945 cm^{-1} for
18 alkali-activated GBFS). This shift was monitored for different curing ages (28, 180, 393
19 days), and is attributed to the formation of the amorphous gel phase after alkaline activation.
20 Samples S0 and S100 were also analysed after 1 year in the natural laboratory conditions and
21 compared to the corresponding reference samples that were sealed for 1 year (without CO_2).
22 Comparing the FTIR spectra's features, there was no significant difference between reference
23 and exposed S0 sample, manifesting that the N-A-S-H gel does not react with ionic carbonic
24 acid in the natural laboratory conditions, as found by Bernal et al. [51]. Only a weak peak at
25 1444 cm^{-1} was found as a new peak that can be assigned to $\nu^3 \text{CO} (\text{CO}_3^{2-})$ band. Similar to

1 sample S0, sample S100 after 1 year in the natural laboratory conditions did not undergo
2 chemical changes, which can be seen from the comparison to the sample that was sealed for 1
3 year, suggesting no carbonation effect on the main structure of the gel. This is attributed to the
4 low porosity of the sample S100 that did not allow CO₂ molecules to diffuse into the material,
5 supported by N₂ adsorption measurements in the section 3.4.

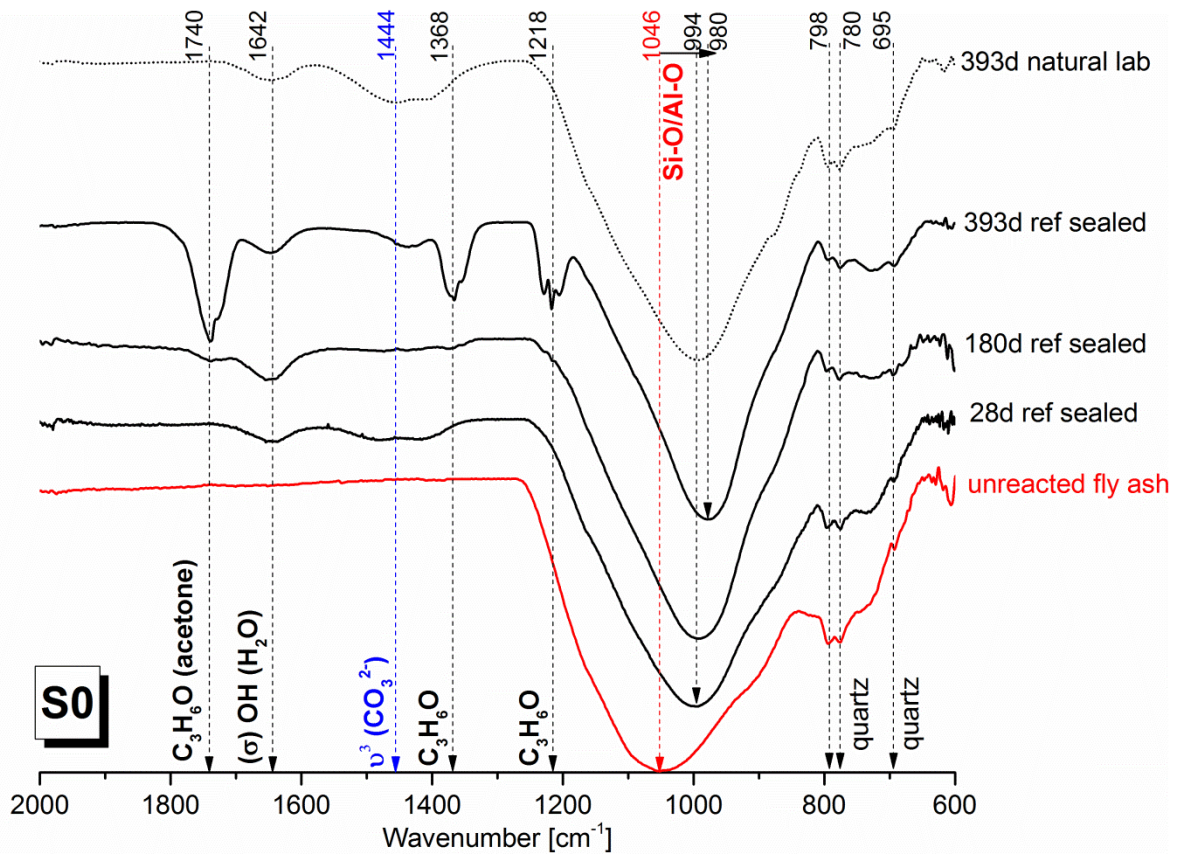
6 Regarding blended pastes (S30, S50, S70), their reference spectra for samples at 28,
7 180, 393 days have the main band assigned to Si-O stretching vibrations of the SiQ²
8 tetrahedra located at 960, 953, 947 cm⁻¹, which shifts to lower wavenumbers with increasing
9 GBFS content, i.e. with increasing Ca/Si ratio, indicating progressive depolymerisation of the
10 silicate chains as reported by Yu et al. [56]. In Fig. 11, the spectra of the samples exposed for
11 1 year in the natural laboratory conditions have the main band that was shifted progressively
12 towards higher wavenumbers from 947 cm⁻¹ to 996 cm⁻¹. The shift to higher wavenumbers
13 indicates the presence of more polymerised units, as the calcium is removed indicating silicate
14 polymerization upon C-(N-)A-S-H gel decalcification. The excess of negative charge in the
15 gel due to Ca²⁺ removal, was balanced through adsorption of alkalis (OH⁻, Na⁺) in the
16 decalcified C-(N-)A-S-H gel and formation of Si-OH or Si-O-Na groups. Condensation of
17 neighbouring groups Si-OH or Si-O-Na into Si-O-Si moves the system towards the
18 equilibrium, forming silicate gel. The very broad absorption bands (900–1200 cm⁻¹) of
19 carbonated samples S30, S50 and S70, indicated the amorphous character of the silicate gel as
20 showed in [57]. Spectra of the carbonated samples S30, S50 and S70 contain also new
21 features, which can be associated with the formation of carbonates with different intensities
22 indicated by the presence of the large bands near 713, 740, 858, 874, 1420 and 1490 cm⁻¹
23 (Fig. 11, Table 5). The intensity of the carbonate peaks are higher in S50 sample comparing to
24 that of S30 and S70 samples. Therefore, S50 sample is the most vulnerable to carbonation.
25 The results are in agreement with SEM-EDX findings.

1 **Table 5**

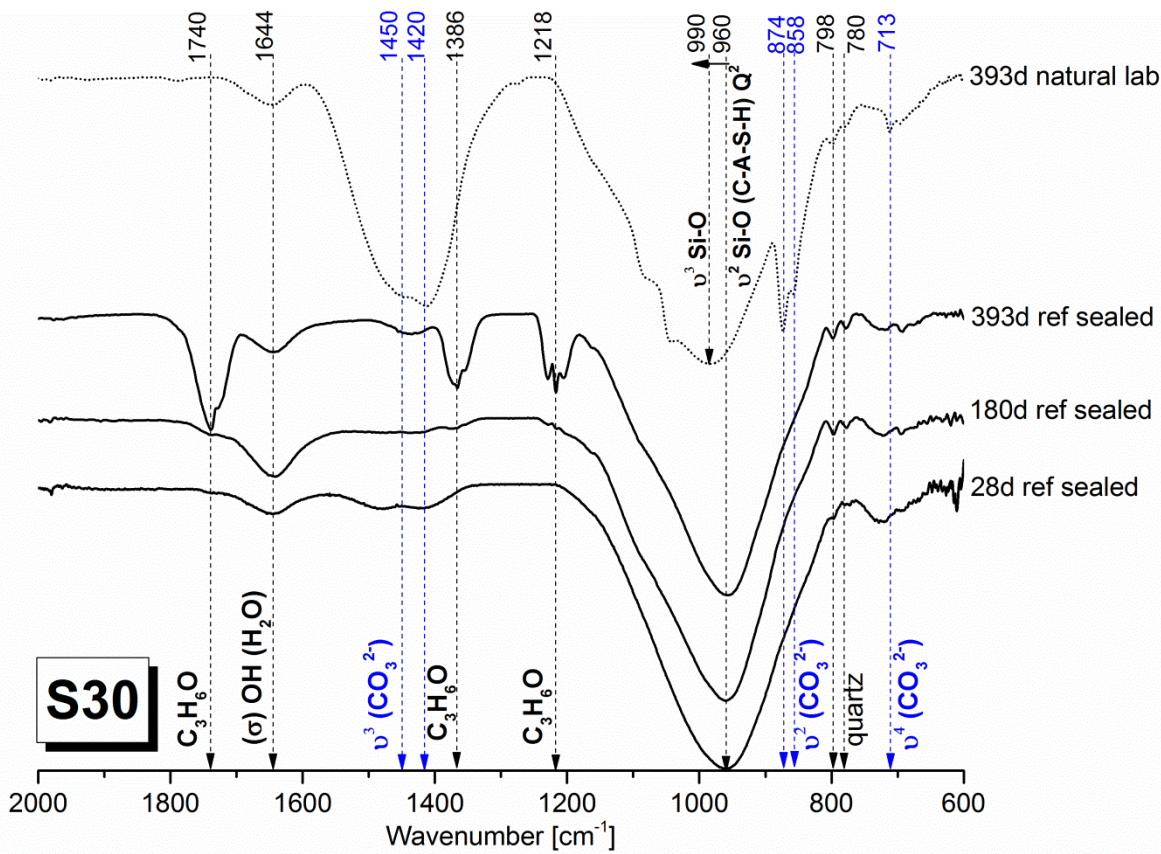
2 Summary of the most present bands for the reference samples sealed for 393 d (denoted as R)
 3 and the samples exposed in the natural laboratory conditions for 393 d (denoted as NLC) (Fig.
 4 11).

Band assignments	FA	GBFS	S0		S30		S50		S70		S100	
	raw	raw	R	NLC	R	NLC	R	NLC	R	NLC	R	NLC
$\nu^4 \text{CO} (\text{CO}_3^{2-})$ (calcite)	-	-	-	-	-	713	-	713	-	713	-	-
$\nu^4 \text{CO} (\text{CO}_3^{2-})$ (vaterite)	-	-	-	-	-	-	-	740	-	740	-	-
$\nu^2 \text{CO} (\text{CO}_3^{2-})$ (vaterite)	-	-	-	-	-	858	-	858	-	858	-	-
$\nu^2 \text{CO} (\text{CO}_3^{2-})$ (vaterite)	-	-	-	-	-	874	-	874	-	874	-	-
$\nu \text{Si-O Q}^2$	-	890	980	994	960	-	953	-	947	-	945	-
$\nu^3 \text{Si-O}$	1050	-	-	-	-	990	-	996	-	995	-	-
$\nu^3 \text{CO} (\text{CO}_3^{2-})$ (vaterite/calcite)	-	-	-	1440	-	1420 1480	-	1420 1480	-	1420 1480	-	-
$\delta \text{OH} (\text{H}_2\text{O})$	-	-	1642	1642	1644	1644	1642	1642	1642	1642	1646	1646

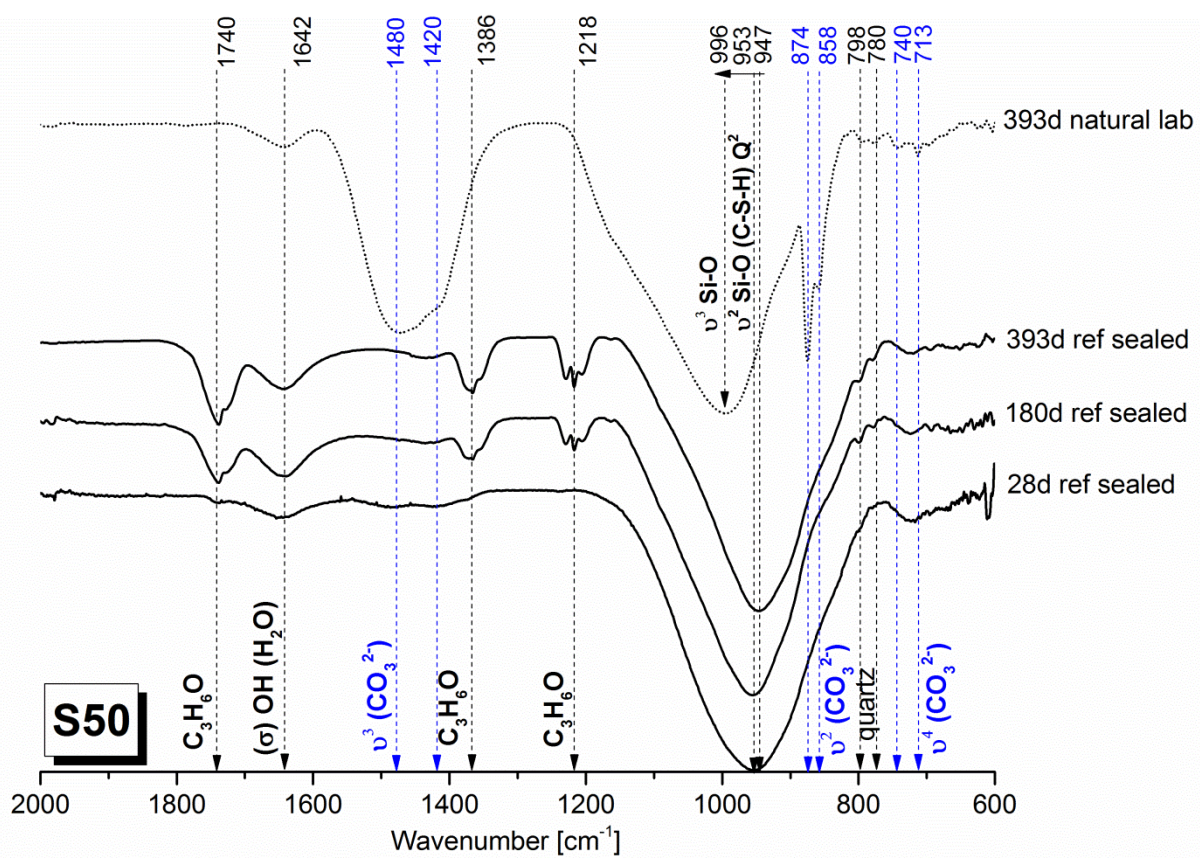
5



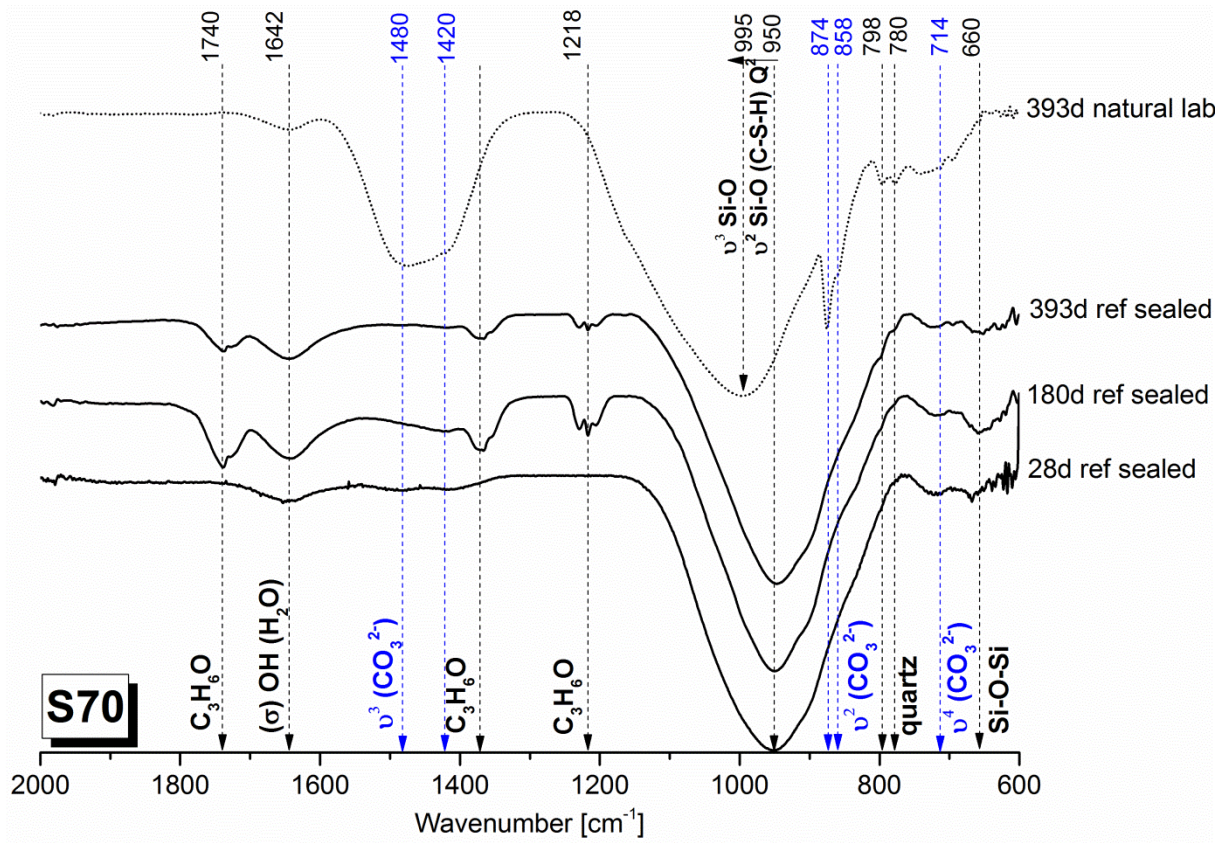
6



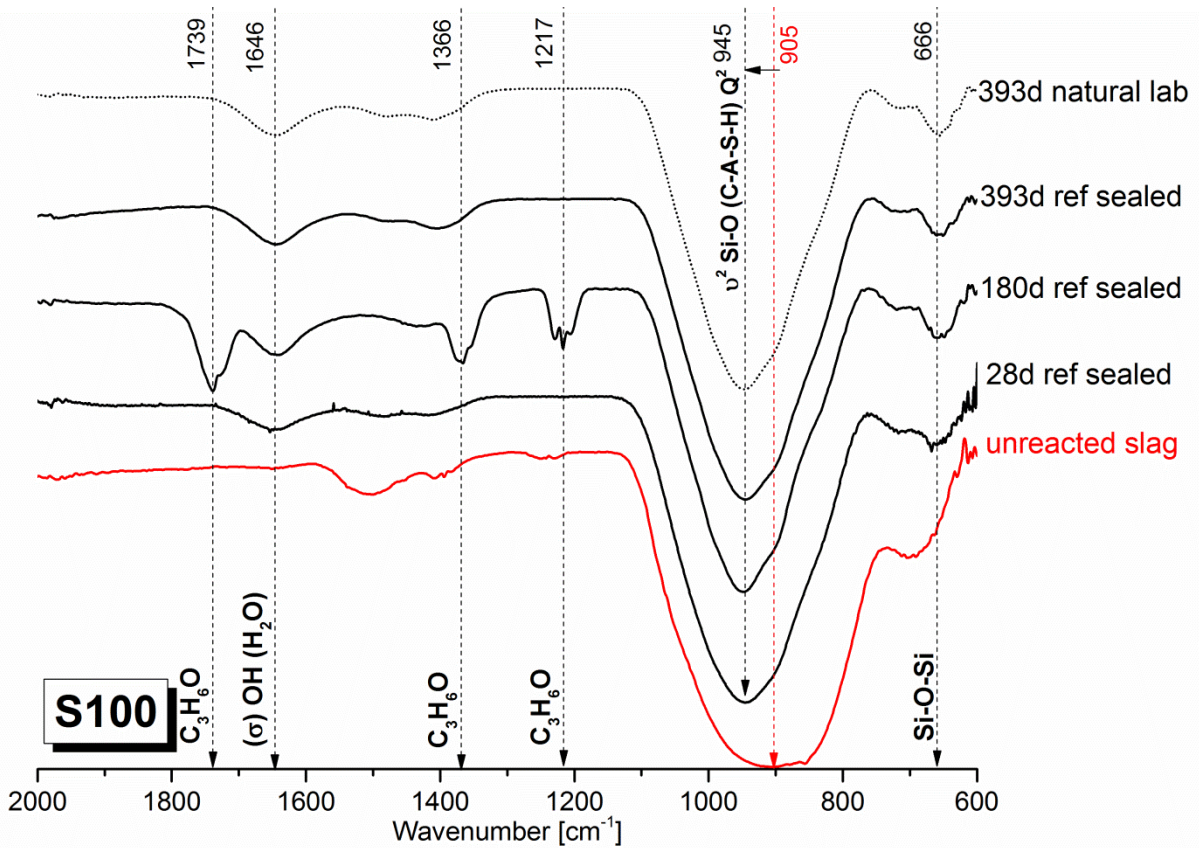
1
2
3



4



1
2
3



4

1 **Fig. 11.** Infrared spectra of alkali-activated pastes.

2

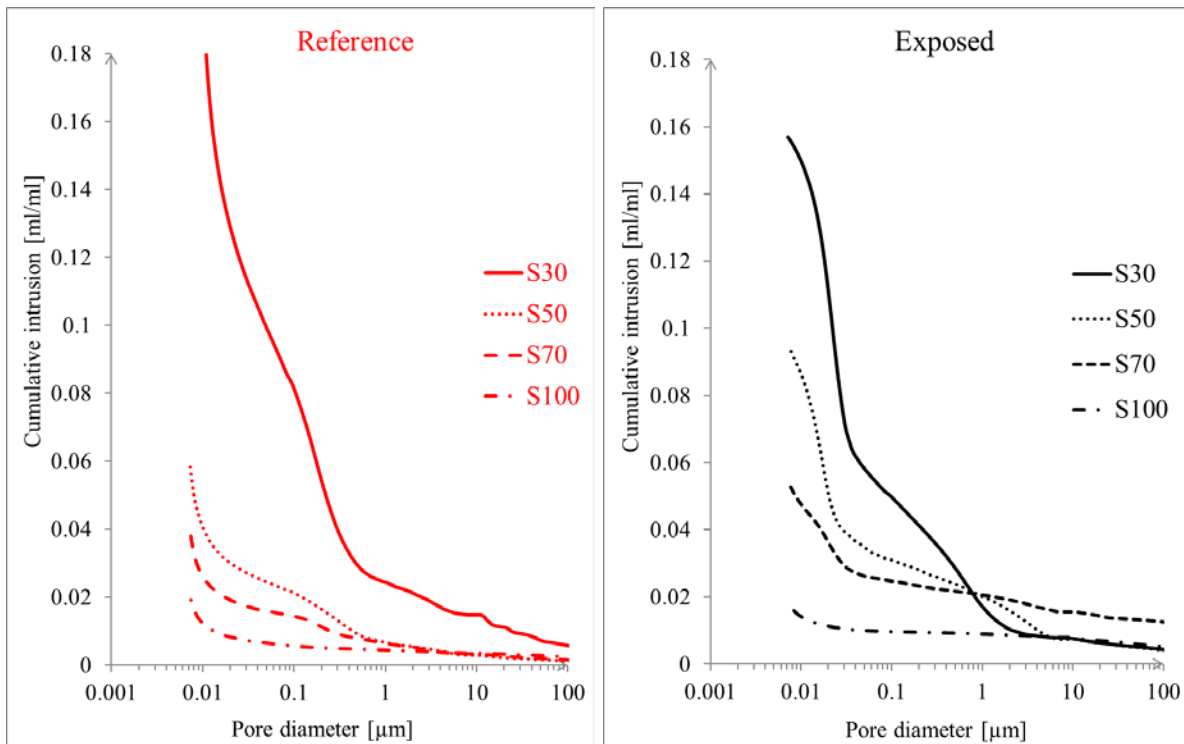
3 3.4. Pore structure by MIP and N₂ adsorption

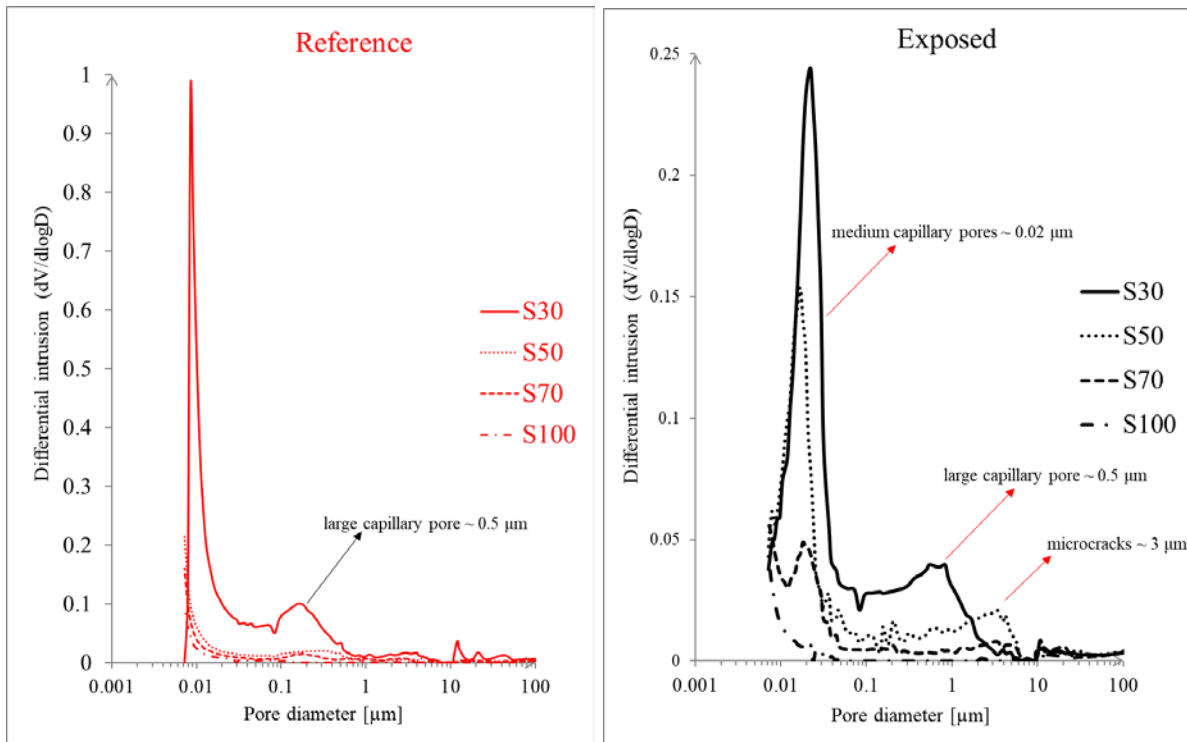
4 Pore size and pore size distribution measurements were performed for the reference
5 pastes and for the pastes exposed in the natural laboratory conditions. The MIP results for all
6 mixtures and the main pore structure characteristics are summarized in Table 6, while
7 cumulative intruded pore volume curves and corresponding pore size distributions obtained
8 for carbonated and reference samples are presented in the Fig. 12. Total porosity and
9 threshold pore diameter of the pastes with higher GBFS content decreases. The physical
10 meaning of a threshold pore diameter reported in Table 6 is that the pores with the diameter
11 greater than this cannot form a connected path through the sample [58]. It should be noted that
12 the threshold pore diameter could not be determined for reference samples and for some of the
13 samples exposed to CO₂ (S70, S100), suggesting very dense microstructures. The MIP tests
14 for sample S100 after 1 year of the exposure, have shown no significant change in the volume
15 of capillary pores, compared to the reference samples (no carbonation). However, sample S0
16 exhibited a decrease in total porosity, probably due to formation of sodium carbonates as
17 found by XRD (Fig. 8) and their precipitation in the pore space. Although, sodium-based
18 carbonates were identified, their content is not enough to justify such a decrease of the total
19 porosity in carbonated S0 sample, compared to the reference S0 sample. It is believed that
20 sodium-based carbonates were leached out during sample preparation due to their high
21 solubility and high porosity of S0 paste (~40% v/v), before the pore structure properties of the
22 samples have been tested. On the other hand, S50 and S70 samples have an increased total
23 porosity (Fig. 12). This increase is attributed to the formation of porous silicate gel after the
24 C-(N-)A-S-H gel has been decalcified. In order to study the effect of carbonation on the gel
25 pore size distribution (PSD) N₂ adsorption method was used.

1 **Table 6**
 2 Capillary pore structure properties by MIP.
 3

Mixtures	Threshold pore access diameter (μm) Reference	Threshold pore access diameter (μm) Carbonated	Total porosity [%] by volume Reference	Total porosity [%] by volume Carbonated
S0	0.120	0.134	30.41	43.72
S30	-	0.03	26.04	26.22
S50	-	0.028	9.404	17.09
S70	-	0.026	6.538	9.66
S100	-	-	3.57	3.38

4





1
2 **Fig. 12.** MIP Capillary pore volume and pore size distribution (reference and exposed samples
3 after 1 year).

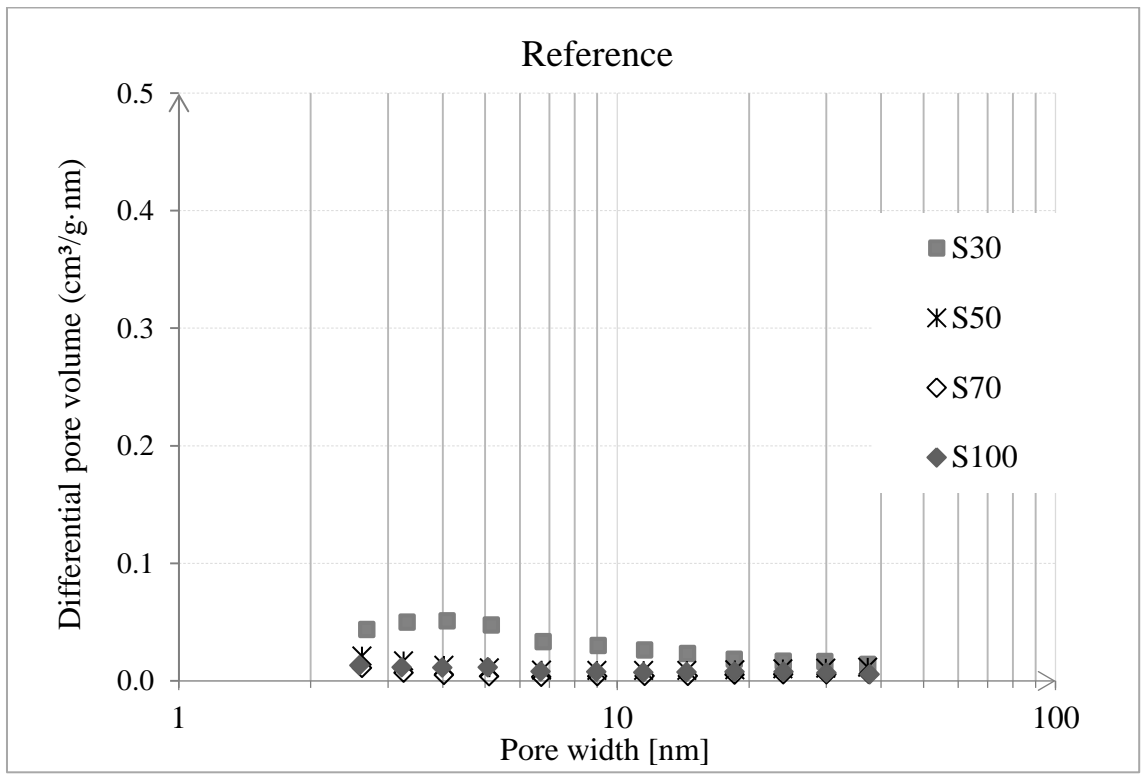
4
5 N₂ adsorption measurements are shown in the Fig. 13. The results are summarized in Table 7.
6 The PSD indicates a dense microstructure for sample S100, where CO₂ can hardly diffuse and
7 react with phases. The gel porosity of the pastes decreases with increasing GBFS content. As
8 the SEM images showed (Fig. 9), there will be more restriction on diffusion in GBFS-rich
9 than through FA-rich pastes. The largest differences in the pore size and volume between
10 reference and exposed samples were found for pastes S30 and S50. The main change is in
11 BET surface area, i.e. increase of the gel pores surfaces (Table 7). For instance, the results
12 have shown that carbonated S50 sample has a significantly higher BET surface area compared
13 to the reference sample. This increase is attributed to the widening of the gel pores due to the
14 gel decalcification and polymerization of silicate chains.

15 **Table 7**
16 Gel pore structure properties by N₂ adsorption, evolution of the BET surface area.

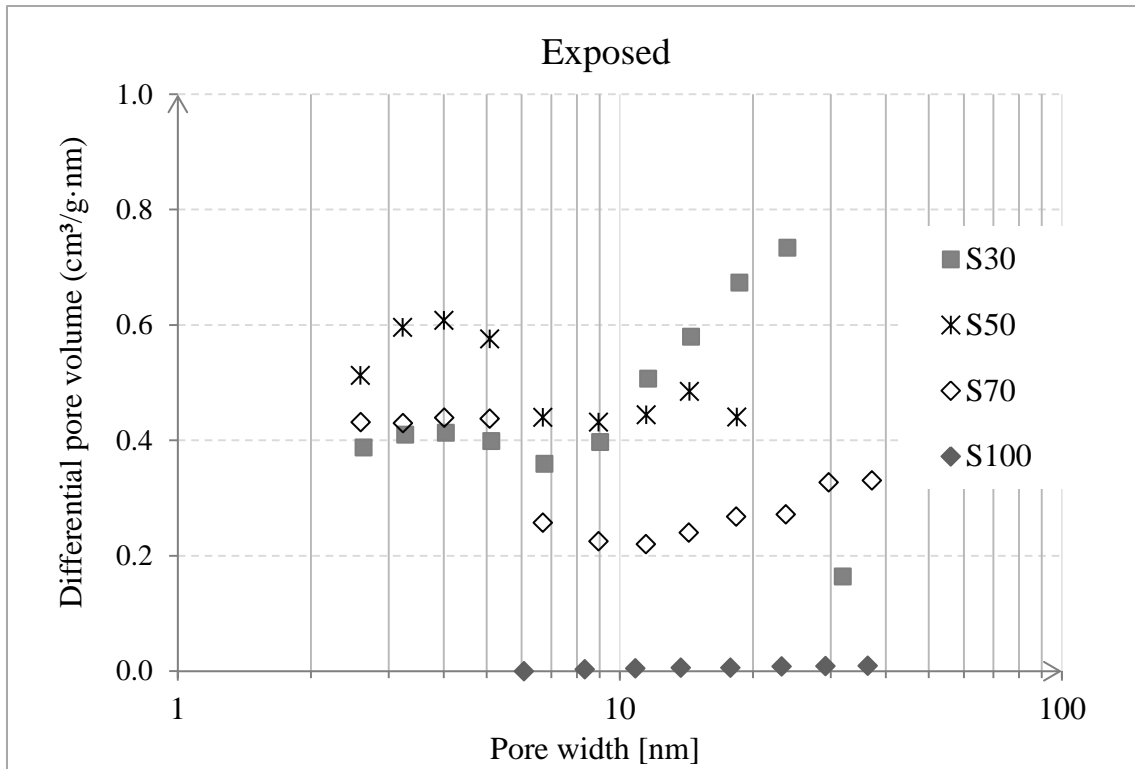
17

Mixtures	Threshold pore access diameter (nm)	Threshold pore access diameter (nm)	BET surface area [m ² /g]	BET surface area [m ² /g]
	Reference	Carbonated	Reference	Carbonated
S0	12	-	15.85	6.71
S30	5.52	7.29	2.58	27.91
S50	6.16	7.47	1.57	34.89
S70	6.57	6.25	0.88	25.1
S100	6.01	-	0.78	0.25

1



2



1
 2 **Fig. 13.** BJH pore size distributions in reference samples (upper photo) and exposed samples
 3 (photo below) after 1 year.

4 3.5. Nanoindentation modulus (E_m)

5 The area of indents is visualized by the optical microscope for the samples S50 (Fig.
 6 14a) and S100 (Fig. 14b). Both mixtures have the grey/brownish background which is the gel
 7 phase. The brightest uneven shaped particles are the unreacted GBFS particles, and the
 8 slightly bright/white particles are partially reacted FA and GBFS particles.

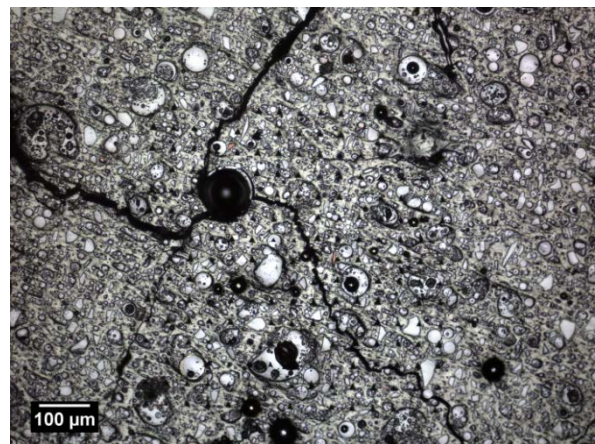
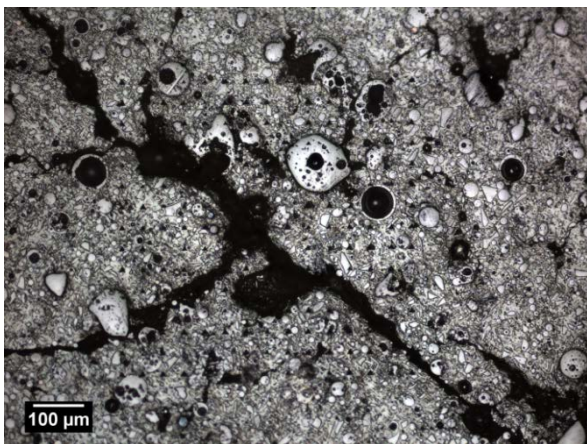


Fig. 14a. Optical microscope photo of S50 sample in the natural laboratory conditions (left: edge) and (right: core).

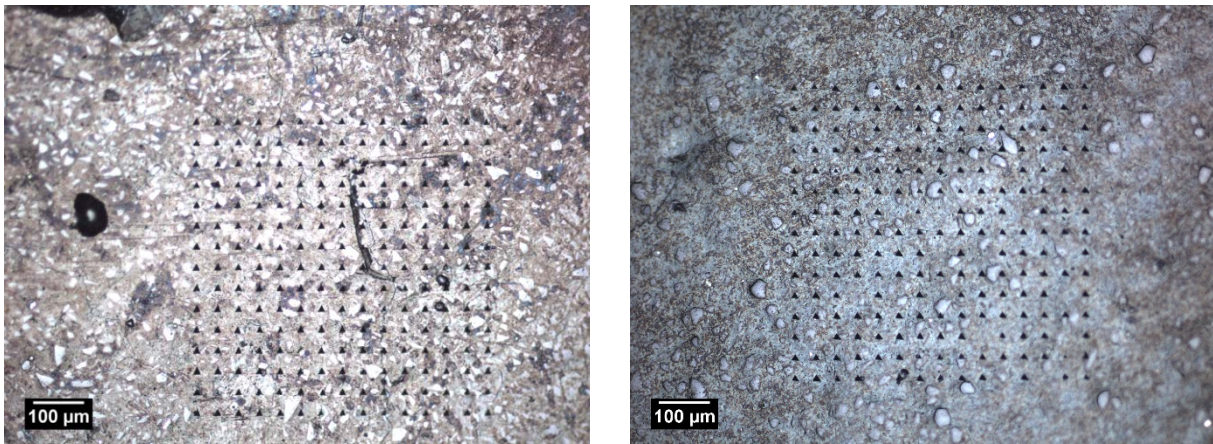


Fig. 14b. Optical microscope photo of S100 sample in the natural laboratory conditions (left: edge) and (right: core).

1 The intermixing of the phases can be expected during the measurements due to
2 inherent heterogenous nature of the studied material. However, the number of indents (200 in
3 this study) should be enough to represent E_m of the phases in the regions of interest. For
4 instance, Fig. 14b shows noncarbonated area of indents in the sample S100. It can be clearly
5 seen that the proportion of the indents printed on the rims between large GBFS particles and
6 the gel, is much less compared to the proportion of the indents printed solely in the gel. When
7 the effect of carbonation on the mechanical properties is tested in a standard way, such as
8 sample bulk testing of compressive strength of concrete [NEN 5988-1999], the error of
9 intermixing is far worse, since such a bulk analysis cannot separate the E_m values for different
10 phases in the system. The advantage of nanoindentation method is that E_m can be locally
11 tested, which otherwise could not be possible with other techniques. The possible error of
12 nanoindentation measurements regarding intermixing of the phases, is reduced by the number
13 of the measurements that were made for each of the areas of interest, noncarbonated and
14 carbonated. A representative SEM images of indents in noncarbonated area (blue triangles) in
15 sample S50 are shown in Fig. 15 (1, 2). In contrast, Fig. 15 (3, 4) show the carbonated areas

1 with a high degree of degradation occurs due to carbonation. The evolution of pores within
2 the microstructure is visible in the vicinity of indents (red triangles) and overall surface. Fig.
3 16 shows a comparison between the results for E_m in the carbonated and noncarbonated
4 indented areas in the form of a histogram. Every histogram represents approximately 200
5 indents from the sample.

6 In this study, four intervals of E_m were defined and linked to the E_m value of four
7 features in the samples; (i) pores, $E_m < 4$ GPa, (ii) carbonated C-(N-)A-S-H gel, $4 < E_m < 21$ GPa,
8 (iii) noncarbonated C-(N-)A-S-H gel, $21 < E_m < 45$ GPa, (iv) unreacted FA and GBFS particles,
9 $E_m > 46$ GPa. The definition of the four intervals defined in this work is based on the results
10 from the literature [25, 34, 59]. Ma [34] has reported E_m for different types of unreacted FA
11 particles. The same FA type was used in this study as a precursor. The E_m of the Ca-rich FA
12 particles was in the range of 75.7–91.2 GPa, the Fe-rich FA particles was 71.0–137.7 GPa, for
13 Al-rich FA particles was between 33.3–65.4 GPa, and Si-rich FA particle presented the elastic
14 modulus of 82.9 GPa. The E_m for GBFS particles and alkali-activated GBFS was found in the
15 study of Puertas et al. [59]. Constantinides and Ulm reported the elastic modulus of C-S-H,
16 and decalcified C-S-H, ranging between 19.5 and 31.8 GPa, 2.2 and 13.2 GPa, respectively
17 [25].

18 Due to the uniform and dense microstructure, the E_m of the S100 sample was not
19 altered under natural carbonation compared to the reference sample. Fig. 16 shows one range
20 of the E_m for sample S100, which indicates its uniform phase composition. Unlike the mixture
21 S100, the blended pastes were carbonated. The results were compared with those of
22 equivalent noncarbonated parts of the samples, except for the paste S0. Due to low reactivity
23 of FA in the S0 paste and consequently its low strength, the preparation of this sample for
24 nanoindentation test was not possible.

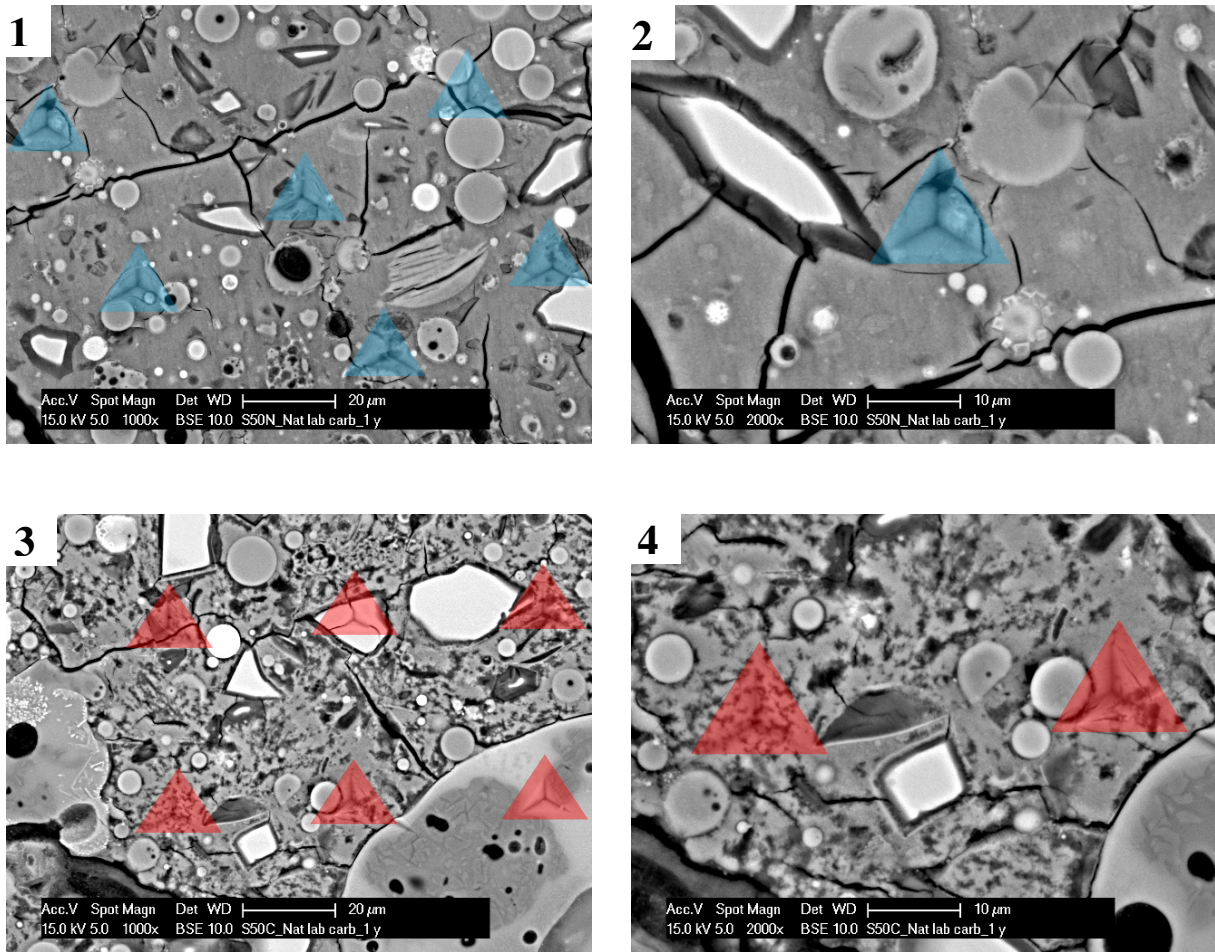


Fig. 15. Visualization of an indentation size for nanoindentation with respect to the noncarbonated (1, 2) and carbonated (3,4) microstructure morphology observed under the SEM.

1 The significant reduction of the E_m was identified in the carbonated pastes S30 and
2 S50, while the reduction of the E_m was of lower extent in paste S70. This can be explained by
3 the lower Ca content (Table 3) in S30 and S50 pastes which results in faster carbonation of
4 the reaction products in S30 and S50, compared to S70 or S100 pastes. On the other hand,
5 pastes S30 and S50 are more porous (Fig. 12, Table 6) compared to the paste S70 or S100,
6 and therefore faster CO_2 diffusion occurs in former. Carbonation mainly causes reduction of
7 the modulus of elasticity in the 5-45 GPa range, where values correspond to the E_m of the gel
8 (Fig. 16). These values shift to lower E_m values after carbonation, as found in the carbonated
9 blended OPC and GBFS cement paste by Çopuroğlu et al. [17]. Modification of the pore

1 structure due to the gel decalcification, is the main reason for E_m reduction, supported by MIP
2 and N_2 adsorption results which showed increase in pore sizes and BET surface area of the
3 carbonated samples compared to the noncarbonated (Table 6 and Table 7).

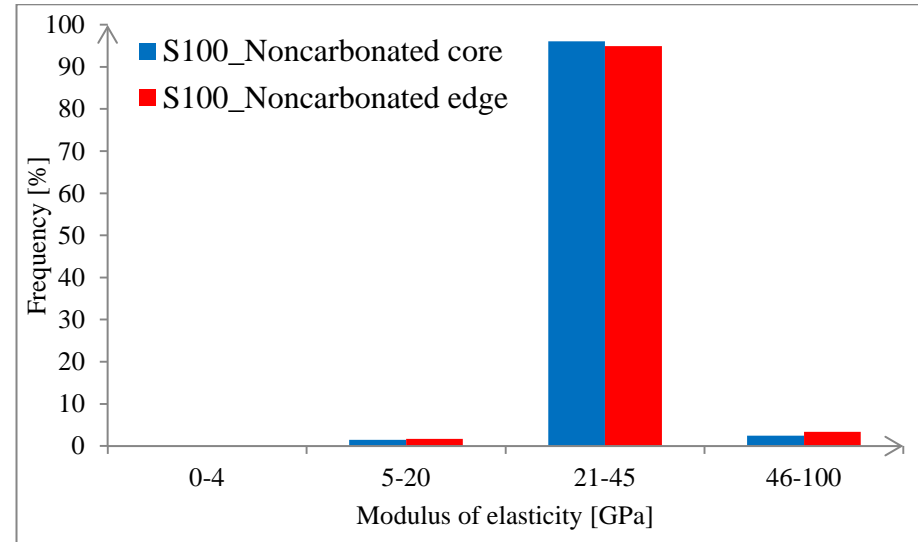
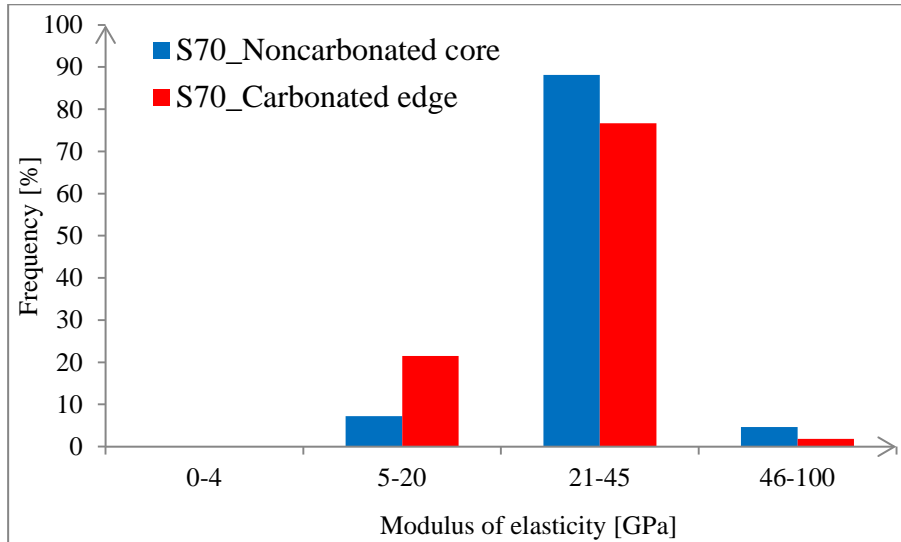
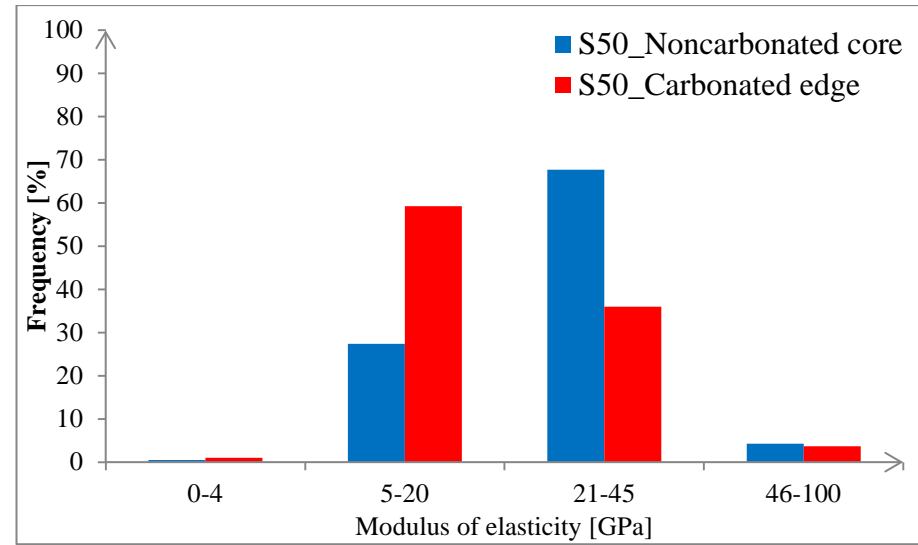
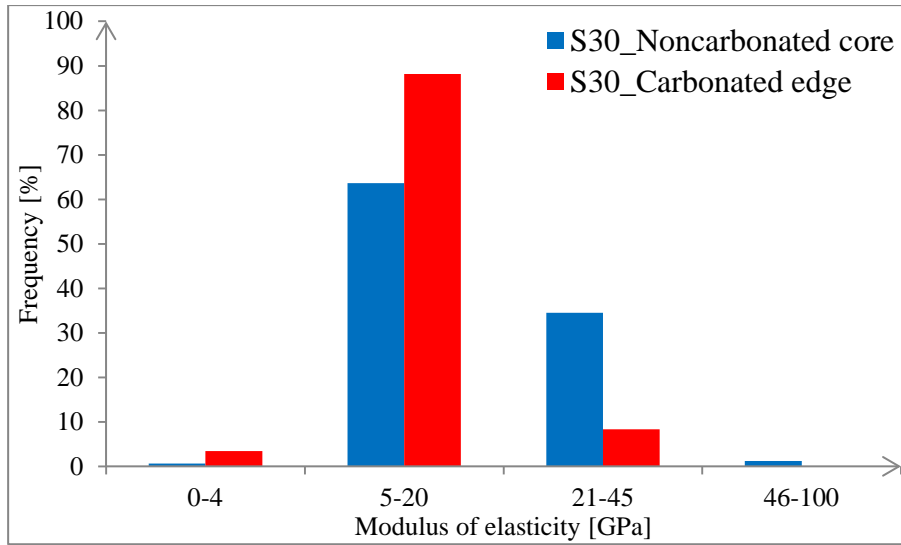


Fig. 16. Effect of natural carbonation on E_m .

4. Implications of natural carbonation in alkali-activated FA and GBFS pastes

The carbonation effects discussed in previous sections have important implications for the understanding of long-term performance in alkali-activated FA and GBFS pastes. In particular, chemical and physical assessments of the microstructure in the studied pastes were a prerequisite for understanding the change of their E_m due to natural laboratory carbonation. The natural laboratory carbonation of the five different paste mixtures resulted in different carbonation depths being governed by their composition and the pore structure in the samples. The results implied that limited carbonation in the GBFS-rich pastes might be a potential advantage in the extension of the service life of AAM. Improved testing of the complex pore structure may be needed for future predictive models.

The reference pastes S30, S50, S70 comprised mainly amorphous C-(N)-A-S-H gel, whilst the carbonated gel in these pastes was composed of calcium carbonates (vaterite and calcite) and silicates. Similar precipitation morphology is found in all blended alkali-activated pastes. Beside calcium carbonates precipitation such as showed by XRD, the polymerization of the silicate chains upon gel decalcification may cause a volumetric change, coarsening the pore structure. The range of the pores in noncarbonated gel (reference) is $0 < r < 50$ nm, whereas gel after carbonation has larger pores, with $3 < r < 1000$ nm. Since microstructure of the reference pastes has mainly gel pores, except S0 and S30 pastes (Fig. 12 and Fig. 13), the CO_2 molecules could not diffuse into the pastes S50, S70 and S100, considering that diffusion and transport of liquid and gas are mainly related to the capillary pores in the matrix. It is believed that the microcracks provided a diffusion of the CO_2 molecules and their dissolution in the pore liquid of the samples S50 and S70. The microcracks are most likely formed due to drying shrinkage considering their width and the depth as shown in the Fig. 17, after the samples were moved from the sealed curing conditions to the natural laboratory conditions. The observations of the microstructure under fluorescent light microscope separated denser

noncarbonated areas form the carbonated, degraded areas in the samples. The pastes emitted high (S0), normal (S30, S50), low (S70), and none (S100) fluorescence suggesting different densities in the noncarbonated and carbonated areas. The areas of the lower density (light green areas, Fig. 17) are where carbonation occurred and where E_m was reduced. It can be also seen that S70 sample has only been carbonated for a few mm along the outermost cracks. Fig. 17 also confirmed that no carbonation took place in the S100 paste.

Although the degradation due to carbonation in this study is investigated on a microscopic scale, the results give insight in large-scale systems such as concrete. The dominant structural failure of the OPC-based concrete due to carbonation, is mostly related to the corrosion of the steel reinforcement embedded in concrete rather than of the binder itself. Therefore, the transport properties of the hardened binder are essential in predicting the service life of structural OPC-based concrete. However, in AAM it is showed that carbonation might not be a cause of corrosion of the embedded steel reinforcement, since the pH in AAM, provided by the high concentrations of the alkali from the activators, can be kept above the value at which corrosion of the steel reinforcement in the concrete initiates, i.e. at the $\text{pH} < 9$ [45]. Therefore, beside testing pH of the carbonated pore solution, and potential corrosion of steel reinforcement embedded in concrete as usually done in OPC-based materials, attention should be drawn to the degradation of the mechanical properties in carbonated AAM. Since the main reaction products in AAM are predominantly amorphous such as shown in this paper by XRD quantification measurements, the reduction of the E_m of the carbonated gel, might be a parameter that has to be considered in the predictive models for service life estimation in AAM due to carbonation effect. In addition, local evaluation of the degraded micromechanical properties of the paste is essential to explain the behaviour of concrete, whereas the change in carbonated paste-aggregate interface will have an additional effect.

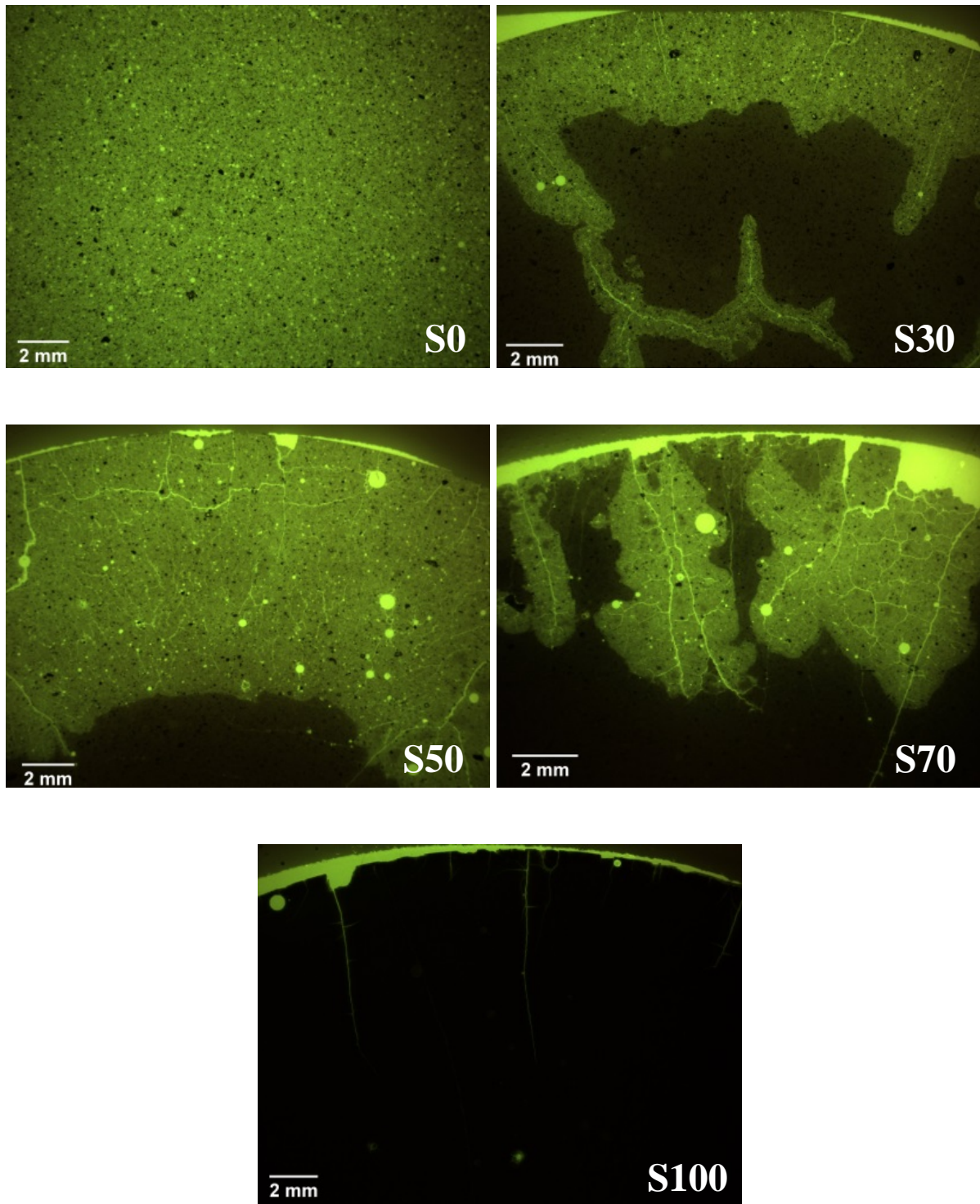


Fig. 17. Fluorescent yellow resin impregnated thin-section samples viewed in reflected fluorescent light, showing the carbonation depth from the top surface toward the core of the samples; noncarbonated matrix is dark grey to black; carbonated matrix, microcracks, voids and pores are light green.

5. Conclusions

The effect of carbonation on pore structure and E_m were studied in the alkali-activated FA and GBFS pastes after exposure in the natural laboratory conditions for 1 year. Results show that the alkali-activated FA (S0) except its pore solution has not carbonated in the studied conditions. Similarly, the alkali-activated GBFS (S100) was highly dense that CO_2 could not diffuse in the sample. N_2 adsorption tests identified the gel pores (with a pore diameter less than 10 nm) to be dominant in the noncarbonated pastes and this technique was more useful for pore structure characterization than the MIP method. The blended pastes were partially carbonated. The carbonation first led to the removal of Ca from the gel, forming vaterite and calcite. Subsequently, an excess of negative charges in the gel due to Ca removal, was balanced through formation of Si-OH or Si-O-Na groups. Condensation of neighbouring Si-OH or Si-O-Na groups into Si-O-Si formed silicate gel as found by ATR-FTIR analyses.

The main change in the pore size distribution occurred in the level of the nanometer pore sizes, whereas the significant increase of the surface area (BET) is identified in the carbonated S30, S50 and S70 pastes. The E_m decreased significantly in the carbonated samples S30 and S50 compared to the corresponding noncarbonated samples, whereas no significant change of the E_m was found in the pastes with 70 and 100 wt.% of GBFS. The potential advantage of using rich GBFS binders is seen in the extension of the service life of AAM.

Acknowledgements

This research was carried out under the project S81.1.13498 in the framework of the Partnership Program of the Materials innovation institute M2i (www.m2i.nl) and the Technology Foundation STW (www.stw.nl), which is part of the Netherlands Organisation for Scientific Research (www.nwo.nl). The authors thank Stefan Melzer from Ceramics

Research Centre (Tata Steel RD&T, Ijmuiden, The Netherlands) for his help with the mineralogy study.

References

1. J.S. van Deventer, J.L. Provis, P. Duxson, D.G. Brice, Chemical research and climate change as drivers in the commercial adoption of alkali activated materials, *Waste Biomass Valorization*. 1(1) (2010) 145-55.
2. J.S. van Deventer, J.L. Provis, P. Duxson, Technical and commercial progress in the adoption of geopolymers, *Miner. Eng.* 29 (2012) 89-104.
3. S.A. Bernal, E.D. Rodríguez, A.P. Kirchheim, J.L. Provis, Management and valorisation of wastes through use in producing alkali-activated cement materials, *J. Chem. Technol. Biotechnol.* 91(9) (2016) 2365-88.
4. F. Pacheco-Torgal, J. Labrincha, C. Leonelli, A. Palomo, P. Chindaprasit, *Handbook of alkali-activated cements, mortars and concretes*, Elsevier, 2014.
5. S.A. Bernal, J.L. Provis, Durability of Alkali-Activated Materials: Progress and Perspectives, *J. Am. Ceram. Soc.* 97(4) (2014) 997-1008.
6. K. Arbi K, M. Nedeljković, Y. Zuo, G. Ye, A review on the durability of alkali-activated fly ash/slag systems: advances, issues, and perspectives, *Ind. Eng. Chem. Res.* 55(19) (2016) 5439-53.
7. T. Bakharev, J.G. Sanjayan, Y.B. Cheng, Resistance of alkali-activated slag concrete to carbonation, *Cem. Concr. Res.* 31(9) (2001) 1277-83.
8. M. Palacios, F. Puertas, Effect of carbonation on alkali-activated slag paste, *J. Am. Ceram. Soc.* 89(10) (2006) 3211-21.
9. F. Puertas, M. Palacios, T. Vázquez, Carbonation process of alkali-activated slag mortars, *J. Mater. Sci.* 41(10) (2006) 3071-82.
10. S.A. Bernal, R.M. de Gutiérrez, A.L. Pedraza, J.L. Provis, E.D. Rodríguez, S. Delvasto, Effect of binder content on the performance of alkali-activated slag concretes, *Cem. Concr. Res.* 41(1) (2011) 1-8.
11. A. Morandau, M. Thiery, P. Dangla, Investigation of the carbonation mechanism of CH and CSH in terms of kinetics, microstructure changes and moisture properties. *Cem. Concr. Res.* 56 (2014) 153-70.
12. R.J. Myers, S.A. Bernal, R. San Nicolas, J.L. Provis, Generalized structural description of calcium–sodium aluminosilicate hydrate gels: the cross-linked substituted tobermorite model, *Langmuir*. 29(17) (2013) 5294-306.
13. I. Soroka, *Portland cement paste and concrete*, 1980.
14. B. Šavija, M. Luković, Carbonation of cement paste: understanding, challenges, and opportunities, *Constr. Build. Mater.* 117 (2016) 285-301.

15. J. Han, G. Pan, W. Sun, C. Wang, D. Cui, Application of nanoindentation to investigate chemomechanical properties change of cement paste in the carbonation reaction, *Science China Technological Sciences*. 55(3) (2012) 616-22.
16. H.S. Shang, T.H. Yi, L.S. Yang. Experimental study on the compressive strength of big mobility concrete with nondestructive testing method, *Adv. Mater. Sci. Eng.* (2012)
17. O. Çopuroğlu, E. Schlangen, Modeling of frost salt scaling, *Cem. Concr. Res.* 38(1) (2008) 27-39.
18. J.J. Chen, Thomas JJ, H.M. Jennings, Decalcification shrinkage of cement paste. *Cem. Concr. Res.* 36(5) (2006) 801-9.
19. S.A. Bernal, R.M. de Gutierrez, J.L. Provis, V. Rose, Effect of silicate modulus and metakaolin incorporation on the carbonation of alkali silicate-activated slags. *Cem. Concr. Res.* 40(6) (2010) 898-907.
20. M. Nedeljkovic, Y.Zuo, K. Arbi, G. Ye, New test method for assessing the carbonation front in alkali-activated fly ash/slag pastes, in *Non-Traditional Cement and Concrete VI*. (2017) Brno, Czech Republic.
21. K. Scrivener, R. Snellings, B. Lothenbach, A practical guide to microstructural analysis of cementitious materials. (2016) CRC Press.
22. J. Kaufmann, Pore space analysis of cement-based materials by combined Nitrogen sorption-Wood's metal impregnation and multi-cycle mercury intrusion. *Cem. Concr. Comp.* 32(7) (2010) 514-522.
23. E.P. Barrett, L.G. Joyner, P.P. Halenda, The determination of pore volume and area distributions in porous substances. I. Computations from nitrogen isotherms. *J. Am. Chem. Soc.* 73(1) (1951) 373-80.
24. A.J. Katz, A.H. Thompson, Quantitative prediction of permeability in porous rock, *Phys. Rev. B.* 34(11) (1986) 8179.
25. G. Constantinides, F.J. Ulm, The effect of two types of CSH on the elasticity of cement-based materials: Results from nanoindentation and micromechanical modeling, *Cem. Concr. Res.* 34(1) (2004) 67-80.
26. O. Bernard, F.J. Ulm, E. Lemarchand, A multiscale micromechanics-hydration model for the early-age elastic properties of cement-based materials, *Cem. Concr. Res.* 33(9) (2003) 1293-309.
27. J.J. Hughes, P. Trtik, Micro-mechanical properties of cement paste measured by depth-sensing nanoindentation: a preliminary correlation of physical properties with phase type, *Mater. Charact.* 53(2) (2004) 223-31.
28. M. Luković, E. Schlangen E, G. Ye, Combined experimental and numerical study of fracture behaviour of cement paste at the microlevel, *Cem. Concr. Res.* 73 (2015) 123-35.
29. B. Šavija, M. Luković M, S.A. Hosseini, J. Pacheco, E. Schlangen, Corrosion induced cover cracking studied by X-ray computed tomography, nanoindentation, and energy dispersive X-ray spectrometry (EDS), *Mater. Struct.* 48(7) (2015) 2043-62.

30. I. Beleña, W. Zhu, Nanoindentation Study of Na-Geopolymers Exposed to High Temperatures, in *Nanotechnology in Construction 3: Proceedings of the NICOM3*, Z. Bittnar, et al., Editors. (2009), Springer Berlin Heidelberg: Berlin, 169-174.
31. J. Němeček, V. Šmilauer, L. Kopecký, Nanoindentation characteristics of alkali-activated aluminosilicate materials, *Cem. Concr. Compos.* 33(2) (2011) 163-70.
32. V. Šmilauer, P. Hlaváček, F. Škvára, R. Šulc, L. Kopecký, J. Němeček, Micromechanical multiscale model for alkali activation of fly ash and metakaolin. *J. Mater. Sci.* 46(20) (2011) 6545-55.
33. S. Das, P. Yang, S.S. Singh, J.C. Mertens, X. Xiao, N. Chawla, N. Neithalath, Effective properties of a fly ash geopolymer: Synergistic application of X-ray synchrotron tomography, nanoindentation, and homogenization models, *Cem. Concr. Res.* 78 (2015) 252-62.
34. Y. Ma, G. Ye, J. Hu, Micro-mechanical properties of alkali-activated fly ash evaluated by nanoindentation, *Constr. Build. Mater.* 147 (2017) 407-16.
35. F.J. Ulm, M. Vandamme, C. Bobko, J. Alberto Ortega, K. Tai, C. Ortiz, Statistical indentation techniques for hydrated nanocomposites: concrete, bone, and shale, *J. Am. Ceram. Soc.* 90(9) (2007) 2677-92.
36. W. Zhu, J.J. Hughes, N. Bicanic, C.J. Pearce, Nanoindentation mapping of mechanical properties of cement paste and natural rocks, *Mater. Charact.* 58(11) (2007) 1189-98.
37. F.J. Ulm, M. Vandamme, H.M. Jennings, J. Vanzo, M. Bentivegna, K.J. Krakowiak, G. Constantinides, C.P. Bobko, K.J. Van Vliet, Does microstructure matter for statistical nanoindentation techniques? *Cem. Concr. Compos.* 32(1) (2010) 92-9.
38. J.J. Chen, L. Sorelli, M. Vandamme, F.J. Ulm, G. Chanvillard, A Coupled Nanoindentation/SEM-EDS Study on Low Water/Cement Ratio Portland Cement Paste: Evidence for C-S-H/Ca(OH)₂ Nanocomposites, *J. Am. Ceram. Soc.* 93(5) (2010) 1484-93.
39. W.C. Oliver, G.M. Pharr, Measurement of hardness and elastic modulus by instrumented indentation: Advances in understanding and refinements to methodology, *J. Mater. Res.* 19(1) (2004) 3-20.
40. W.M. Jung, S.H. Kang, W.S. Kim, C.K. Choi, Particle morphology of calcium carbonate precipitated by gas-liquid reaction in a Couette-Taylor reactor. *Chem. Eng. Sci.* 55(4) (2000) 733-747.
41. C.Y. Tai, P.C. Chen, Nucleation, agglomeration and crystal morphology of calcium carbonate. *AIChE J.* 41(1) (1995) 68-77.
42. D. Kralj, L. Brečević, A.E. Nielsen, Vaterite growth and dissolution in aqueous solution I. Kinetics of crystal growth. *J. Cryst. Growth*, 104(4) (1990) 793-800.
43. J. Hostomsky, A.G. Jones, Calcium carbonate crystallization, agglomeration and form during continuous precipitation from solution. *J. Phys. D: Appl. Phys.* 24(2) (1991) p.165.
44. Z. Šauman, Long-term carbonization of the phases 3CaO·Al₂O₃·6H₂O and 3CaO·Al₂O₃·SiO₂·4H₂O. *Cem. Concr. Res.* 2(4) (1972) 435-446.

45. S.A. Bernal, J.L. Provis, D.G. Brice, A. Kilcullen, P. Duxson, J.S. van Deventer, Accelerated carbonation testing of alkali-activated binders significantly underestimates service life: the role of pore solution chemistry. *Cem. Concr. Res.* 42(10) (2012) 1317-1326.
46. Hidalgo, A., Domingo, C., Garcia, C., Petit, S., Andrade, C. and Alonso, C., Microstructural changes induced in Portland cement-based materials due to natural and supercritical carbonation. *J. Mater. Sci.* 43(9) (2008) 3101-3111.
47. C.E. White, L.L. Daemen, M. Hartl, K. Page, Intrinsic differences in atomic ordering of calcium (aluminosilicate) hydrates in conventional and alkali-activated cements. *Cem. Concr. Res.* 67 (2015) 66-73.
48. K. Sisomphon, O. Çopuroğlu, A.L. Fraaij, Development of blast furnace slag mixtures against frost salt attack, *Cem. Concr. Compos.* 32(8) (2010) 630-8.
49. C. Famy, K.L. Scrivener, A.K. Crumbie, What causes differences of CSH gel grey levels in backscattered electron images? *Cem. Concr. Res.* 32(9) (2002) 1465-71.
50. A.E. Morandau, C.E. White, In situ X-ray pair distribution function analysis of accelerated carbonation of a synthetic calcium–silicate–hydrate gel. *J. Mater. Chem. A* 3(16) (2015) 8597-8605.
51. S.A. Bernal, J.L. Provis, B. Walkley, R. San Nicolas, J.D. Gehman, D.G. Brice, A.R. Kilcullen, P. Duxson, J.S. van Deventer, Gel nanostructure in alkali-activated binders based on slag and fly ash, and effects of accelerated carbonation. *Cem. Concr. Res.* 53 (2013) 127-44.
52. M. Nedeljkovic, K. Arbi, Y. Zuo, G. Ye, Physical properties and pore solution analysis of alkali-activated fly ash-slag pastes. In: 2016 Proceedings pro113: International RILEM Conference Materials Systems and Structures in Civil Engineering 2016 (MSSCE 2016), Denmark
53. M.B. Haha, B. Lothenbach, G.L. Le Saout, F. Winnefeld, Influence of slag chemistry on the hydration of alkali-activated blast-furnace slag-Part I: Effect of MgO. *Cem. Concr. Res.* 41(9) (2011) 955-963.
54. N.J. Clayden, S. Esposito, A. Aronne, P. Pernice, Solid state ²⁷Al NMR and FTIR study of lanthanum aluminosilicate glasses, *J. Non-Cryst. Solids.* 258(1) (1999) 11-9.
55. A. Fernández-Jiménez, A. Palomo, Mid-infrared spectroscopic studies of alkali-activated fly ash structure, *Microporous and mesoporous materials*, 86(1) (2005) 207-14.
56. P. Yu, R.J. Kirkpatrick, B. Poe, P.F. McMillan, X. Cong, Structure of calcium silicate hydrate (C-S-H): Near-, Mid-, and Far-infrared spectroscopy, *J. Am. Ceram. Soc.* 82(3) (1999) 742-8.
57. D. Dimas, I. Giannopoulou, D. Papias, Polymerization in sodium silicate solutions: a fundamental process in geopolymerization technology. *J. Mater. Sci.* 44(14) (2009) 3719-3730.

58. G. Ye, Experimental study and numerical simulation of the development of the microstructure and permeability of cementitious materials, Ph.D. thesis, Delft University of Technology, The Netherlands, 2003.
59. F. Puertas, M. Palacios, H. Manzano, J.S. Dolado, A. Rico, J. Rodríguez. A model for the CASH gel formed in alkali-activated slag cements, *J. Eur. Ceram. Soc.* 31(12) (2011) 2043-56.